This manuscript has been submitted for publication in Agricultural and Forest Meteorology. Please note that, the manuscript is currently under review and has yet to be formally accepted for publication. Subsequent versions of this manuscript may have slightly different content. If accepted, the final version of this manuscript will be available via the 'Peer-reviewed Publication DOI' link

STEEP: a remotely-sensed energy balance model for evapotranspiration estimation in seasonally dry tropical forests

Ulisses A. Bezerra[a*], John Cunha[a], Fernanda Valente[b], Rodolfo L. B. Nóbrega[c,d], João M. Andrade[e], Magna S. B. Moura[f], Anne Verhoef[g], Aldrin M. Perez-Marin[h], Carlos O. Galvão[a]

[a]Federal University of Campina Grande, Centre for Natural Resources and Technology, Campina Grande, Brazil

[b]Forest Research Centre (CEF), School of Agriculture, University of Lisbon, Tapada da Ajuda, 1349-017 Lisbon, Portugal

[c]University of Bristol, School of Geographical Sciences, University Rd, Bristol, BS8 1SS, UK

[d]Imperial College London, Georgina Mace Centre for the Living Planet, Department of Life Sciences, Silwood Park Campus, Buckhurst Road, Ascot, SL5 7PY, UK

[e]Federal University of Pernambuco, Department of Civil and Environmental Engineering, Recife, Brazil

[f]Empresa Brasileira de Pesquisa Agropecuária, Embrapa Semiárido, Petrolina, Brazil

[g]The University of Reading, Department of Geography and Environmental Science, UK

[h]Instituto Nacional do Semiárido/Núcleo de Desertificação e Agroecologia, Campina Grande, Brazil

*Corresponding author: ulisses.alencar@estudante.ufcg.edu.br; ulisses.alencar17@gmail.com

Highlights

- STEEP is a RS-based SEB model from a one-source bulk transfer equation for SDTF
- STEEP includes improved representations of phenology and soil moisture for SDTF
- STEEP is tested against eddy covariance data from the largest SDTF in South America
- STEEP exhibits satisfactory metrics and outperforms SEBAL, MOD16, and PMLv2

Abstract

Improvement of evapotranspiration (ET) estimates using remote sensing (RS) products based on multispectral and thermal sensors has been a breakthrough in hydrological research. In large-scale applications, methods that use the approach of RS-based surface energy balance (SEB) models often rely on oversimplifications. The use of these models for Seasonally Dry Tropical Forests (SDTF) has been challenging due to incompatibilities between the assumptions underlying those models and the specificities of this environment, such as the highly contrasting phenological phases

or ET being mainly controlled by soil–water availability. We developed a RS-based SEB model from a one-source bulk transfer equation, called STEEP. Our model uses the Plant Area Index to represent the woody structure of the plants in calculating the moment roughness length. In the aerodynamic resistance for heat transfer, the parameter kB^{-1} was included, correcting it with RS soil moisture. Besides, the remaining λET in endmembers pixels was quantified using the Priestley-Taylor equation. We implemented the algorithm on Google Earth Engine, using worldwide free data. Four sites with eddy covariance data located in the Caatinga, the largest SDTF in South America, in the Brazilian semiarid region, were used to evaluate our model. Our results show that STEEP based on the specific characteristics of the STDF, such as phenology and soil moisture, increased the accuracy of ET estimates without requiring any additional climatological information. This improvement is more pronounced during the dry season, which, in general, ET for these SDTF is overestimated by traditional SEB models, as happened with the Surface Energy Balance Algorithms for Land (SEBAL). The STEEP model had similar or superior behaviour and performance statistics relative to global ET products (MOD16 and PMLv2). This work contributes to an improved understanding of the drivers and modulators of the energy and water balances at local and regional scales in SDTF.

Keywords: Sensible heat flux, Aerodynamic resistance for heat transfer, Surface energy balance, Caatinga, Google Earth Engine

1. Introduction

Quantifying evapotranspiration (ET) is one of the largest research challenges in hydrology because ET is driven by a complex combination of atmospheric, vegetation, edaphic and terrain characteristics (Wang et al., 2016; Bhattarai et al., 2017). The traditional techniques to quantify ET, e.g. Bowen ratio or eddy covariance system (EC), are limited to areas up to ~10 km² (Allen et al., 2011; Anapalli et al., 2016; Mcshane et al., 2017; Mallick et al., 2018; Chu et al., 2021). Over the past decades, models based on satellite remote sensing (RS) data have been increasingly developed and applied to estimate ET for multiple temporal and spatial scales (Anderson et al., 2011; Chen and Liu, 2020). RS-based surface energy balance (SEB) models estimate ET in terms of energy per unit area (W/m²), i.e. by latent heat flux, λET, where λ is the latent heat of vaporization of

water (Shuttleworth, 2012; Barraza et al., 2017; Trebs et al., 2021). SEB models obtain λET by subtracting the soil heat (G) and sensible heat (H) fluxes from the net radiation (R_n). Estimates of R_n obtained with RS data have been improving, and this flux can nowadays be estimated with acceptable precision (Allen et al., 2011; Ferreira et al., 2020). The $G:R_n$ ratio can be predicted with reasonable accuracy through the use of empirical relationships with soil, vegetation, and temperature characteristics (Bastiaanssen, 1995; Murray and Verhoef, 2007; Allen et al., 2011; Danelichen et al., 2014). Challenges in estimating λET as a residual of the energy balance are mostly associated with the uncertainties in H (Gokmen et al., 2012; Paul et al., 2014; Mohan et al., 2020a, b; Costa-Filho et al., 2021). The bulk heat transfer calculation that is used to compute H involves variables related to the temperature gradient and to the aerodynamic resistance for heat transfer (*rah*). If any of these variables are poorly estimated, the performance of SEB models will be reduced (Verhoef et al., 1997a, b; Su et al., 2001; Gokmen et al., 2012; Costa-Filho et al., 2021; Liu et al., 2021; Trebs et al., 2021).

The difference between the aerodynamic surface temperature and air temperature (dT) drives H. However, the lack of techniques to measure the aerodynamic surface temperature required strategies to use the radiometric land surface temperature (LST) as an alternative. Bastiaanssen et al. (1998), when creating the Surface Energy Balance Algorithms for Land (SEBAL), proposed that dT can be estimated with a linear relationship on LST. This requires identifying areas with contrasting extreme conditions in terms of cover and humidity, e.g., dry bare and well-watered soil surfaces, commonly known as hot/dry and cold/wet endmembers, respectively. The sensible heat transfer equation, in conjunction with the surface energy balance in hot/dry and cold/wet endmembers, allows one to obtain the coefficients of the linear relationship between dT and LST. Bastiaanssen et al. (1998) proposed the selection of endmembers by assuming that H in the cold/wet endmember and λET in the hot/dry endmember are zero. However, these assumptions are not necessarily valid (Singh and Irmak, 2011; Singh et al., 2012). The cold/wet endmember refers to an area with a well-irrigated crop surface having ground fully covered by vegetation, so it can be assumed that a non-negligible amount of sensible heat can still be generated by such a surface. Similarly, for the hot/dry endmember, an area dominated by bare soil, there may be a remaining λET resulting from antecedent rainfall events. Some studies have quantified H and λET in hot/dry and cold/wet

endmembers (Trezza, 2006; Allen et al., 2007; Singh and Irmak, 2011); they have shown that this quantification produces a better approximation of daily ET.

Based on the Monin-Obukhov similarity theory, *rah* is defined as a function of the momentum (*z0m*) and heat (*z0h*) roughness lengths. Theoretically, the sum of the zero plane displacement height (*d0*) together with *z0h* defines the level of the effective source of sensible heat (Thom, 1972; Chehbouni et al., 1996; Gokmen et al., 2012) and, therefore, *z0h* constitutes one of the most crucial parameters for the accurate calculation of *H* (Verhoef et al., 1997a; Su et al., 2001). However, as *z0h* cannot be measured directly, it is commonly calculated via the dimensionless parameter kB^{-1} formulated to express the excess resistance of heat transfer compared to momentum transfer (Owen and Thomson, 1963). In RS-based SEB models, oversimplifications are present in the calculation of *rah*, e.g. different land use types are represented by the same values for *z0h* (Bastiaanssen et al., 2005; Allen et al., 2007) and kB^{-1} (Bastiaanssen et al., 1998), or the values for the aerodynamic parameters are kept constant in time and space. However, these parameters should not be considered constant, nor set to zero, as this can lead to large inaccuracies in the estimates of *H* (Verhoef et al., 1997a) and, consequently, of λET (Liu et al., 2007; Paul et al., 2014; Liu et al., 2021). Studies have shown that kB^{-1} typically ranges from 1 to 12, depending on the dominant surface coverage (Kustas et al., 1989a; Troufleau et al., 1997; Verhoef et al., 1997a; Lhomme et al., 2000; Su et al., 2001). Studies confirm that if appropriate values of kB^{-1} are used, *H* can be accurately estimated using LST via the bulk transfer method (Stewart et al., 1994; Su et al., 2001; Jia et al., 2003; Paul et al., 2013).

Another problem with RS-based SEB models is that these methods are imprecise when applied to non-agricultural environments, such as forests, deserts, sparse savannahs or rangelands and riparian systems, because of the heterogeneous nature of the vegetation, terrain, soils, and water availability in these environments. This causes the flux estimates obtained with the SEB method, and the underlying aerodynamic parameters, to be highly variable (Allen et al., 2011; Gokmen et al., 2012; Barraza et al., 2017; Chen and Liu, 2020; Costa-Filho et al., 2021). This is especially true in Seasonally Dry Tropical Forests (SDTF) regions, where there is a large spatio-temporal variation in vegetation density, in vegetation structural parameters such as canopy height, crown shape and branching, and water availability. SDTF are an important tropical biome and one

of the most threatened ecoregions of the world (Moro et al., 2015; Pennington et al., 2018). SDTF are broadly defined as forest formations in tropical regions characterised by marked seasonality in rainfall distribution, resulting in a prolonged dry season that usually lasts five or six months (Pennington et al., 2009; Paloschi et al., 2020). The most extensive contiguous areas of SDTF are in the neotropics, comprising more than 60% of the remaining global stands of this vegetation (Miles et al., 2006; Queiroz et al., 2017). The physiognomies exhibited by SDTF are heterogeneous, with vegetation ranging from tall forests with closed canopies to scrublands rich in succulents and thorn-bearing plants (Moro et al., 2015; Paloschi et al., 2020). SDTF foliage patterns are adapted to the intense climate and water seasonality, which is highly dependent on interannual climate variability (Alberton et al., 2017; Medeiros et al., 2022). The vegetation drops most leaves during the dry season, and the first rainfall events trigger a rapid leaf growth in the wet season (Alberton et al., 2017; Paloschi et al., 2020; Medeiros et al., 2022). SDTF are being rapidly degraded (12% between 1980 and 2000), highlighting an urgent priority for their conservation (Moro et al., 2015; Maia et al., 2020). The risks faced by SDTF mainly stem from anthropogenic disturbance effects, which range from local habitat loss to global climate change, leading to biodiversity loss and reductions in biomass (Allen et al., 2017; Maia et al., 2020).

Application of SEB models to estimate evapotranspiration over SDTF has been challenging due to the incompatibility between the existing assumptions of the models and the specificities of these forests. Precipitation seasonality is the primary phenological regulator of SDTF (Moro et al., 2016; Campos et al., 2019; Paloschi et al., 2020), and land-cover patterns show distinct intra- and inter-annual spectral responses (Cunha et al., 2020; Andrade et al., 2021; Medeiros et al., 2022). Therefore, biophysical remotely-sensed variables, such as Normalized Difference Vegetation Index (NDVI) and surface albedo, which are usually used to select the endmembers, exhibit high spatial and temporal variability in SDTF, which causes ET estimates from the SEB models to lack fidelity (Silva et al., 2019). Selection of suitable roughness parameters such as *z0m*, *d0*, and kB^{-1} is important for the correct quantification of the energy balance in SDTF. However, these parameters are more challenging to obtain in SDTF than for evergreen forests, as in addition to vegetation height, other characteristics such as plant density, above-ground plant structure and the strong seasonality of phenology (Alberton et al., 2017; Miranda et al., 2020; Paloschi et al., 2020) have a considerable

effect on the turbulent transfer in these forests. Another key issue is how to verify the results of SEB methods due to the scarcity, in many regions, of terrestrial observations and the uneven spatiotemporal distribution of monitoring data. SEB models may not satisfactorily represent ET in regions with sparse vegetation and high climatic seasonality, such as SDTF (Senkondo et al., 2019; Laipelt et al., 2021; Melo et al., 2021). The main reason is that these methods have generally been evaluated and/or parameterized using sites located in other ecosystems and climates in North America, Europe, Australia, East Asia, and in agricultural regions that have characteristics quite distinct from SDTF (Melo et al., 2021). Therefore, a better quantification of ET, especially in regions with high climatic seasonality, will help to design better water management policies that will be able to deal with the effects of climate variability, land use/cover and climate changes (Lima et al., 2021).

We hypothesise that a SEB model that improves or considers estimates of *z0m*, kB^{-1}, and therefore of rah for the SDTF will improve *H* and ET estimates of these forests. To test this assumption, we introduce a novel calibration-free SEB model based upon a one-source bulk transfer equation, herein referred to as Seasonal Tropical Ecosystem Energy Partitioning (STEEP). The STEEP model aims to improve *H* and ET estimates for STDF by incorporating the woody structure of plants through the Plant Area Index (PAI), and soil moisture obtained by remote sensing to help represent the seasonality of the aerodynamic and surface variables that drive the energy fluxes. In addition, our approach when calculating *dT* uses the concept of the linear relationship in LST. To obtain its coefficients, we compute, in the hot/dry and cold/wet endmembers, *H* by the surface energy balance, and the remaining λET through the principle of the Priestley-Taylor equation. STEEP is designed to take advantage of the extensive free database available on the Google Earth Engine (GEE) cloud computing environment. STEEP is herein evaluated at the field scale against four flux towers in the Caatinga, the largest continuous SDTF in the Americas. Additionally, the model was compared with SEBAL and two consolidated global ET products: MOD16 (Mu et al., 2011; Running et al., 2017) and PMLv2 (Zhang et al., 2019).

2. Methodology

2.1 Study areas and respective data

The study concerns the Brazilian Caatinga, the largest continuous SDTF in the Americas, located between the Equator and the Tropic of Capricorn (about 3 and 18° south), in the Brazilian semiarid region. It covers an area of about 850,000 km² (Silva et al., 2017a; Andrade et al., 2021; Brazil MMA, 2021). The climate in the Caatinga is characterized by high air temperatures (around 26° to 30° C) and high potential evapotranspiration (1,500 to 2,000 mm/year) coupled with low annual rainfall (300 to 800 mm/year, normally concentrated in 3–6 months) with high intra- and inter-annual variability in space and time, and a long dry season which sometimes lasts up to 11 months in some areas of Caatinga (Moro et al., 2016; Miranda et al., 2018; Paloschi et al., 2020). The Caatinga vegetation has at least thirteen physiognomies ranging from woods to sparse thorny shrubs, morphologically adapted to resist water stress and high air temperatures (Araújo et al., 2009; Silva et al., 2017a; Marques et al., 2020; Miranda et al., 2020), and it has been identified as one of the most biodiverse SDTF regions globally (Pennington et al., 2006; Santos et al., 2014; Koch et al., 2017). Still, the Caatinga and other SDTF are among the least studied ecoregions compared to tropical forests and savannas (Santos et al., 2012; Koch et al., 2017; Tomasella et al., 2018; Borges et al., 2020). Only 1% of the Brazilian Caatinga area is legally protected (Koch et al., 2017).

We used data from four sites located in the Caatinga (Fig. 1 and Table 1). The surrounding areas of each of our study sites — which exceeds these EC towers footprints — are homogeneously covered by Caatinga vegetation (Fig. S1). Located on crystalline terrain (Fig. 1a), these Caatinga sites have soils with highly variable properties, ranging from fertile (those with a clayey texture) to poor (those soils that are sandier). However, most soils of the SDTF are typically shallow and stony (i.e. Entisols, Alfisols, and Ultisols; WRB, 2006), retaining water only for a short period between rainfall events and after the rainy season (Moro et al., 2015; Queiroz et al., 2017). The wet and (dry) seasons from the sites PTN are concentrated in Jan–Apr (May-Dec; Souza et al., 2015); SNN in Jan–May (June–Dec; Marques et al., 2020); SET in Nov–Apr (May–Oct; Silva et al., 2017b) and CGR in Mar–July (Aug–Feb; Oliveira et al., 2021). The climate of the four observation sites is semi-arid, type BSh (Fig. 1b) according to the Köppen climate classification (Alvares et al., 2013).

Eddy covariance data, covering several periods from 2011 to 2020 (Fig. 1c), were used to evaluate the modelled ET and *H*. The four sites were instrumented with five flux towers equipped with three-dimensional ultrasonic anemometers (CSAT3, Campbell Scientific Inc., Logan, UT, USA

in all the sites except CGR 2020) and open-path infrared gas analysers (LI-7500, LI-COR Inc., Lincoln, NE, USA, in the PTN site, or EC150, Campbell Scientific Inc., Logan, UT, USA, in the SET, SNN, and CGR 2014 sites). In the more recent experiment (CGR 2020), the flux tower was equipped with an IRGASON (Campbell Scientific Inc., Logan, UT, USA) that integrates the two sensors in just one instrument. ET data for the PTN, SNN and SET sites have been previously described; they underwent standard procedures to ensure their quality and were published by Melo et al. (2021). Observations at the CGR site were collected through two micrometeorological towers, located in a dense Caatinga area within the Brazilian National Institute of Semiarid (INSA) experimental area, a 300 ha forest reserve with different stages of regeneration. The first tower (height of 7 m) was active between the years of 2014 and 2017, as described in Oliveira et al. (2021). The second tower (height of 15 m) is part of the Caatinga Observatory (OCA) and includes an EC system that has been collecting data since 2020. The OCA is a laboratory maintained by the Federal University of Campina Grande and INSA. *H* data for the PTN, SNN and CGR sites have been obtained from the respective principal investigators, while data for the SET site have been obtained from the AmeriFlux network (Antonino, 2019). For the retrieval of λET and *H*, LoggerNet software (Campbell Scientific, Inc., Logan, UT, USA) was used in order to transform 10 Hz raw data into 30 min binaries. Afterwards, EdiRe software (Campbell Scientific Inc., Logan, UT, USA) was used to process the high-frequency data, averaging every 30 min. The data from the EC flow towers in CGR have previously gone through standard procedures to ensure their quality. Detailed information on data processing, quality control, and post-processing can be found in Campos et al. (2019) and Cabral et al. (2020). The raw data from the CGR flux tower were processed by Easy-flux data processing software (Campbell Scientific Inc., Logan, UT, USA). In addition, data for any day with rainfall greater than 0.5 mm were removed. The daily ET was calculated using the daily average λET.

234 Table 1. List of EC-equipped flux tower observation sites in the study area.

Sites	State of Brazil	Mean annual of rainfall (mm)[1]	Site average elevation (m)	Main tree species	Location (Lon;Lat)	Data availability	Wet / Dry Seasons	Main reference
Petrolina (PTN)	Pernambuco	428.6	395	*Commiphora leptophloeos, Schinopsis brasiliensis, Mimosa tenuiflora, Cenostigma microphyllum, Sapium glandulosum*	-40.3212; -9.0465	Jan–Dec 2011	Jan-Apr / May-Dec	Souza et al. (2015)
Serra Negra do Norte (SNN)	Rio Grande do Norte	629.5	205	*Caesalpinia pyramidalis, Aspidosperma pyrifolium, Anadenanthera colubrina, Croton blanchetianus*	-37.2514; -6.5783	Jan–Dec 2014	Jan-May / June-Dec	Marques et al. (2020)
Serra Talhada (SET)	Pernambuco	648	465	*Mimosa hostilis, Mimosa verrucosa, Croton sonderianus, Anadenthera macrocarpa, Spondias tuberosa*	-38.3842; -7.9682	Jan–Dec 2015	Nov-Apr / May-Oct	Silva et al. (2017b)
Campina Grande (CGR)	Paraíba	777	490	*Croton blanchetianus, Mimosa ophthalmocentra, Poincianella pyramidalis, Allophylus quercifolius, Mimosa sp.* [2]	-35.9750; -7.2798	Jan–Dec 2014	Mar-July / Aug-Feb	Oliveira et al. (2021)
Campina Grande (CGR)	Paraíba	777	490	*Croton blanchetianus, Mimosa ophthalmocentra, Poincianella pyramidalis, Allophylus quercifolius, Mimosa sp.* [2]	-35.9763; -7.2805	Jan–Dec 2020	Mar-July / Aug-Feb	This study

[1] Rainfall Data Sources: Brazilian National Institute of Meteorology (INMET) and Pernambuco State Agency for Water and Climate (APAC).

[2] Barbosa et al. (2020).

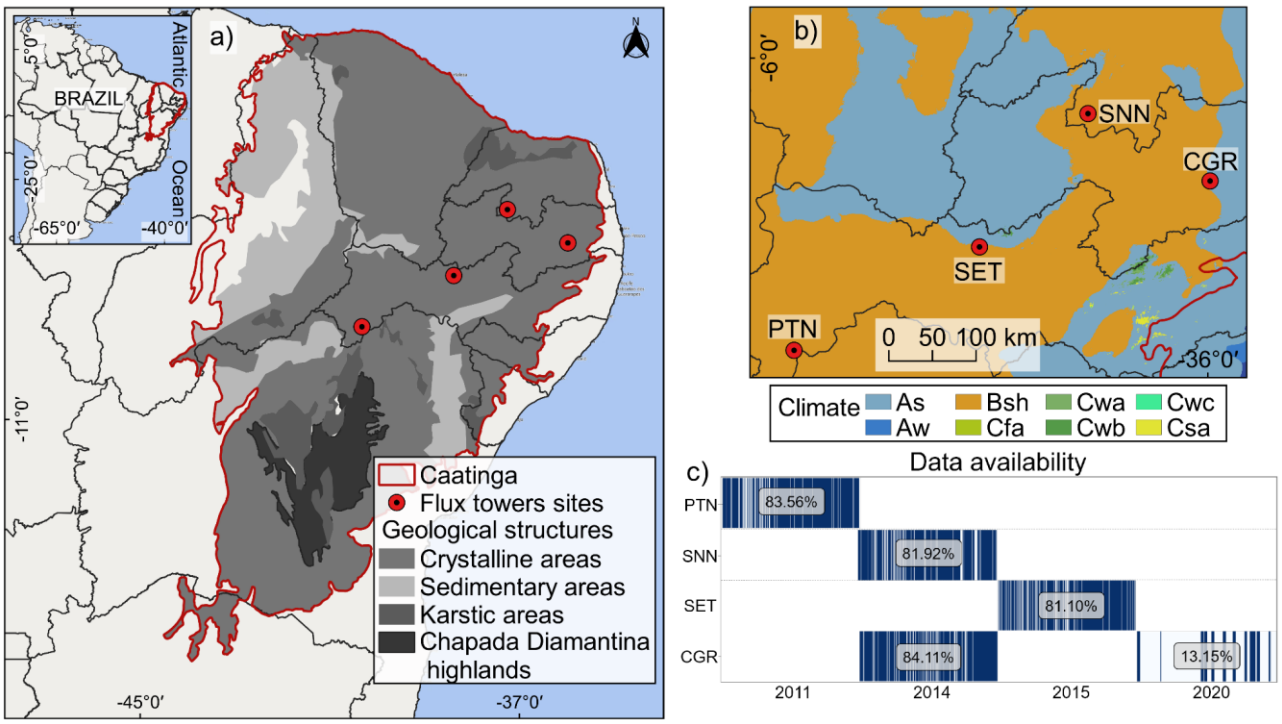

Figure 1. Location of flux tower observation sites in Caatinga. a) Geographical overview of the Caatinga (Moro et al., 2015), b) Köppen's climate classification map:Tropical zone with dry summer (As), Tropical zone with dry winter (Aw), Dry zone semi-arid low latitude and altitude (Bsh), Humid subtropical zone without dry season and with hot summer (Cfa), Humid subtropical zone with dry winter and hot summer (Cwa), Humid subtropical zone with dry winter and temperate summer (Cwb), Humid subtropical zone with dry winter and short and cool summer (Cwc), Humid subtropical zone with dry summer and hot (Csa), according to Alvares et al. (2013) and c) Data availability on the observation sites after procedures to ensure their quality.

2.2 The Seasonal Tropical Ecosystem Energy Partitioning (STEEP) model

SEB models have been applied in many parts of the world (Mohan et al., 2020a). The one-source SEB models that are most commonly found in the literature are SEBAL (Bastiaanssen et al., 1998), Surface Energy Balance System (SEBS; Su, 2002), Mapping EvapoTranspiration at high Resolution with Internal Calibration (METRIC; Allen et al., 2007), and Operational Simplified Surface Energy Balance (SSEBop; Senay et al., 2013). As in other SEB models, STEEP performs the energy balance at the time of satellite overpass (instantaneous) to obtain λET as the surface energy balance residual. The computation of R_n and G, necessary to get λET, followed the procedures described in Ferreira et al. (2020) and Bastiaanssen et al. (2002), respectively, but with input data from the

Moderate-Resolution Imaging Spectroradiometer (MODIS) sensor. *H* was calculated following the methods described in Table 2: using *rah* and *dT*, both traditionally applied in SEB models, but also focusing on peculiarities of SDTF that have never been considered in other SEB models. In this proposed version, *rah* was described according to Verhoef et al. (1997a) and Paul et al. (2013), which requires, among other parameters/variables, the momentum roughness length (*z0m*), the zero plane displacement height (*d0*), the dimensionless parameter kB^{-1}, and the atmospheric stability corrections (Paulson, 1970). *z0m* is influenced by a range of plant structural properties, e.g. vegetation height, breadth and vegetation drag coefficients, and spacing (or density). *z0m* is commonly computed as a function of Leaf Area Index (LAI; Verhoef et al., 1997b; Liu et al., 2021). However, most SDTF plants spend a substantial part of the year without leaves; under these conditions, *z0m* should be derived from information on dimensions of trunks, stems, and branches. Since LAI is only related to leaf cover quantity and variability, it cannot represent the woody plant structure without leaves (Miranda et al., 2020). Therefore, the Plant Area Index (PAI), which is the total above-ground plant area, i.e. leaves and woody structures, was used to represent plant structures in the computation of *z0m* and *d0*.

To incorporate the conditions of water variability in the forest system in the calculation of sensible heat we applied the procedure described in Gokmen et al. (2012) that corrects the kB^{-1} equation presented in Su et al. (2001), incorporating soil moisture obtained by remote sensing. The canopy conductance profiles are the link between soil moisture and sensible/latent heat flux. The source of sensible/latent heat moves vertically throughout the canopy as a function of plant water stress (Gokmen et al., 2012; Bonan et al., 2021), which affects heat roughness length, and, therefore, kB^{-1} and *rah*. Thus, when there is a reduction in soil moisture, there is also a reduction in the value of *rah* and, consequently, an increase of *H* and a decrease in λET. Furthermore, to calculate *dT*, we used the linear relationship on LST, using the assumption of extreme contrast in terms of cover and soil wetness (hot/dry and cold/wet endmembers) to determine the linear relationship coefficients. However, in the hot/dry and cold/wet endmembers pixels, *H* was computed by the surface energy balance (Allen et al., 2007), and the remaining λET was incorporated through the Priestley-Taylor (1972) equation and plant physiological constraints following the approach in Singh and Irmak (2011) and French et al. (2015). PAI and soil moisture time series used in our study can be seen in Fig. S2.

The references for the methods and equations adopted to formulate the STEEP model can be found in Table 2 and Appendix A, respectively. For illustration purposes, Table 2 also shows the references for the methods for one of the most widely used RS SEB models, the SEBAL model.

Table 2. References for the methods used in the STEEP and SEBAL models to obtain the sensible heat flux.

Variable/Parameter	STEEP	SEBAL
Aerodynamic resistance for heat transfer (*rah*)	Verhoef et al., 1997a; Paul et al., 2013	Bastiaanssen et al., 2002; Laipelt et al., 2021
Roughness length for momentum transfer (*z0m*)	Verhoef et al., 1997b; Paul et al., 2013, replacing LAI with PAI	Bastiaanssen et al., 2002; Laipelt et al., 2021
Zero plane displacement height (*d0*)	Verhoef et al., 1997b; Paul et al., 2013	-
Plant Area Index (PAI)	Miranda et al., 2020	-
Parameter kB^{-1}	Su et al., 2001	uses *z0h* with constant value (0.1); Bastiaanssen et al., 2002
Correction of soil moisture by remote sensing in kB^{-1}	Gokmen et al., 2012	-
Calculation of the *H* and the remaining λET in endmembers pixels	Allen et al., 2007; Singh and Irmak, 2011; French et al., 2015	Calculation of the *H* in the hot/dry endmember only; Bastiaanssen et al., 2002

2.3 Algorithm implementation and processing

We implemented STEEP on the Google Earth Engine (GEE) cloud computing environment (Gorelick et al., 2017) using the Python API (version 3.6). Statistical analyses to evaluate the performance of the models were also conducted in Python and implemented in the Jupyter programming environment. The Python package geemap (Wu, 2020) enabled the integration of Python with the GEE environment, and the hydrostats package (Roberts et al., 2018) was used for the statistical evaluation of the performance of the models.

We designed the application of the model to take advantage of the data available on GEE (Table 3). The remote sensing datasets were derived from MODIS sensor products, the Shuttle Radar Topography Mission (SRTM; Farr et al., 2007), and the Global Forest Canopy Height product provided vegetation height (Potapov et al., 2021). The climate data necessary to run the model, i.e. wind speed, air temperature, relative humidity, shortwave radiation, and net thermal radiation at the surface, were sourced from the ERA5-Land reanalysis product (Muñoz Sabater, 2019). For data

regarding soil moisture, we used the Global Land Data Assimilation System (GLDAS) product (Rodell et al., 2004). CHIRPS precipitation product (Funk et al., 2015) was used to estimate the daily rainfall amount at the sites evaluated.

Table 3. Description of the datasets available on the GEE platform used in the research.

Product	GEE ID	Bands/variables	Time coverage	Spatial resolution	Temporal resolution
MCD43A4.006	MODIS/006/MCD43A4	B1–B7	Feb 2000–present	0.5 km	1 day
MOD09GA.006	MODIS/006/MOD09GA	SolarZenith	Feb 2000–present	1 km	1 day
MOD11A1.006	MODIS/006/MOD11A1	LST_Day_1km; Emis_31, Emis_32	Mar 2000–present	1 km	1 day
SRTM	USGS/SRTMGL1_003	Elevation	Feb 2000	0.03 km	-
ERA5-Land	ECMWF/ERA5_LAND/HOURLY	dewpoint_temperature_2m, temperature_2m, u_component_of_wind_10, v_component_of_wind_10m, surface_net_solar_radiation_hourly, surface_net_thermal_radiation_hourly	Jan 1981–present	0.1°	1 hour
GLDAS	NASA/GLDAS/V021/NOAH/G025/T3H	SoilMoi0_10cm_inst	Jan 2000–present	0.25°	3 hours
Global Forest Canopy Height, 2019	users/potapovpeter/GEDI_V27	-	Apr 2019	0.03 km	-
CHIRPS	UCSB-CHG/CHIRPS/DAILY	Precipitation	Jan 1981–present	0.05°	1 day
MOD16A2.006	MODIS/006/MOD16A2	ET	Jan 2001–present	0.5 km	8 days
PML_V2	projects/pml_evapotranspiration/PML/OUTPUT/PML_V2_8day_v016	Es, Ec, Ei	Feb 2000–present	0.5 km	8 days

The presence of clouds or instrumental malfunctioning of orbital sensors can cause gaps in data. To reduce the loss of information due to missing data, we chose to use the MODIS MCD43A4

reflectance product. By combining reflectance data from MODIS sensors aboard the AQUA and TERRA satellites and modelling the anisotropic scattering characteristics using sixteen-day quality observations, the MCD43A4 product represents the daily dynamics of the Earth's surface without missing data (Schaaf and Wang, 2015). Daily surface reflectance data from the MCD43A4 product were used to obtain the surface albedo and vegetation indices (NDVI and PAI) needed to run STEEP. Thus, the surface albedo data and the vegetation indices show a low percentage of missing data. To compose the LST time series, we used data from MOD11A1, and to fill its missing data, a filter with the average value for a monthly window was applied. This procedure is similar to the method proposed by Zhao et al. (2005) and it is also used by the MOD16 algorithm to generate the continuous global ET (Mu et al., 2011).

Following the approach in comparable studies, STEEP algorithm processing was conducted with automatic selection of endmembers pixels (Bhattarai et al., 2017; Silva et al., 2019; Laipelt et al., 2021). Like Silva et al. (2019), we used the biophysical variables NDVI, surface albedo and LST to automate selection of the endmembers, but we applied different criteria. For the hot/dry endmember selection, the first step consisted of selecting those pixels whose surface albedo values are between the 50 and 75% quantiles, and with NDVI values greater than 0.1 and less than the 15% quantile. After this first selection, a refinement is applied by selecting only those pixels from this first set that have LST values between the 85 and 97% quantiles. Using the set of pixels that met these criteria, the median values of R_n, G, LST and *rah* were calculated to establish a single value for each variable and describe the characteristics of the hot pixel. We applied a similar procedure to select the cold/wet endmember but with different limits (Table 4). The procedure for finding endmembers was conducted daily. To execute the model and conduct the selection of endmembers, we used an area of interest (AOI), also known as domain size. AOI was defined as a square area with 1000-km sides within the Caatinga domain and centred on the tower coordinates of each site. Cheng et al. (2021), for example, applied the SEBAL using MODIS data in China and used an AOI of 1200-km x 1200-km.

Table 4. Methodology used for the selection of endmembers pixels.

Endmembers

	Hot/dry pixel	Cold/wet pixel
Step 1	Q50% < surface albedo < Q75% and 0.10 < NDVI < Q15%	Q25% < surface albedo < Q50% and NDVI > Q97%
Step 2	of the pixels of the 1st Step, select pixels with Q85% < LST < Q97%	of the pixels of the 1st Step, select pixels with LST < Q20%
Step 3	Of the set of pixels that met the previous steps, the median values of R_n, G, LST and *rah* were calculated to establish a single value for each variable and describe the characteristics of endmembers	

Q = quantile.

2.4 Analysis of the algorithms' performance

We used SEBAL as a reference RS SEB model for comparison with STEEP. SEBAL is one of the most applied SEB models since the algorithm uses a minimal number of in situ measurements compared to similar models, e.g. METRIC and SSEBop, and is considered a suitable choice for evapotranspiration estimates over cropped areas and in the context of water resource management (Kayser et al., 2022). Applications with SEBAL have been conducted in the Caatinga as in the studies of Teixeira et al. (2009), Santos et al. (2020), Costa et al. (2021), and Lima et al. (2021). Implementations of the SEBAL algorithm are popular on several computing platforms, e.g. GRASS-Python (Lima et al., 2021); Google Earth Engine (Laipelt et al., 2021); Python (Mhawej et al., 2020), following the formulations described in Bastiaanssen et al. (1998) and Bastiaanssen et al. (2002). The SEBAL version implemented in this work followed those presented by Bastiaanssen et al. (2002), Costa et al. (2021) and Laipelt et al. (2021). The remote sensing datasets and endmembers pixels selection for SEBAL were the same as described in STEEP.

ET and *H* estimates from STEEP and SEBAL were evaluated against the eddy covariance measurements of the corresponding tower. Here, the modelled values were extracted for the pixel representing the EC tower for each observation site. The footprint fetches for PTN, SET, SNN is less than 500 m (Silva et al., 2017b; Campos et al., 2019; Santos, et al., 2020). We assume a similar footprint for CGR due to its similarity in terms of wind characteristics and terrain slope compared to the other sites. Moreover, the surrounding areas of each of our study sites (Fig. S1) — which exceeds these EC towers footprints — are homogeneously covered by Caatinga vegetation. We evaluated daily ET values, and instantaneous hourly *H* values more specifically with the modelled/measured *H*

value at 11:00 am local time (GMT-3), considering this is the closest time to the satellite's overpass. Additionally, the STEEP model was compared with two consolidated global ET products available on GEE: MODIS Global Terrestrial Evapotranspiration A2 version 6 (MOD16; Mu et al., 2011; Running et al., 2017) and Penman-Monteith-Leuning model version 2 global evaporation (PMLv2; Zhang et al., 2019); both products have a pixel resolution of 500 m (Table 3). The algorithm used in MOD16 is based on the Penman-Monteith equation and driven by MODIS remote sensing data with Modern-Era Retrospective analysis for Research and Applications (MERRA; Mu et al., 2011). In MOD16 ET is the sum of soil evaporation (Es), canopy transpiration (Tc) and wet-canopy evaporation (Ec) and is provided as eight-day *cumulative* values. More details about MOD16 can be found in Mu et al. (2011) and Running et al. (2017). The global PMLv2 product involves a biophysical model based on the Penman-Monteith-Leuning equation which also uses MODIS remote sensing data, but with meteorological reanalysis data from GLDAS as model inputs. As in MOD16, ET in PMLv2 is also the sum of Es, Tc and Ec but is provided as eight-day *average* values. To make MOD16 and PMLv2 values compatible, ET of PMLv2 was multiplied by eight. Details about PMLv2 can be found in Gan et al. (2018) and Zhang et al. (2019). We accumulated the daily ET measured at the observation sites, i.e. derived from EC data, and ET modelled with STEEP for the same eight-day time periods to make them compatible with the temporal resolution of the MOD16 and PMLv2 datasets. The average of the measured daily values over each eight-day time period (even if there were missing values within this period) was multiplied by eight to calculate the observed 8-day ET. To match the time steps of STEEP and MOD16/PMLv2 ET values, the 8-day average of the evaporative fraction (EF) was multiplied by the daily net radiation over those 8 days, assuming that EF can be considered constant in each of these periods. Then the ET was summed over the 8-day interval. Finally, we also compared the modelled ET (by STEEP and the two global products) with the observed ET, only in the 8-day periods when no field-observed data was missing. However, with this criterion the number of observations dropped dramatically.

The STEEP and SEBAL models and global ET products were evaluated with five performance metrics (Table 5). A combination of performance metrics is often used to assess the overall performance of models because a single metric provides only a projection of a certain aspect of the error characteristics (Chai and Draxler, 2014). Root mean square error (*RMSE*) is commonly used

388 to express the accuracy of the results with the advantage that it presents error values in the same
389 units of the variable analysed; optimal values are close to zero (Hallak and Pereira Filho, 2011).
390 Coefficient of determination (R^2) represents the quality of the linear trend between observed and
391 simulated data and ranges from 0 to 1; high values indicate better model performance. Nash–
392 Sutcliffe efficiency (*NSE*) indicates the accuracy of the model output compared to the average of the
393 referred data (*NSE* = 1 is the optimal value; Nash and Sutcliffe, 1970). Concordance correlation
394 coefficient (*ρc*) is a measure that evaluates how well bivariate data falls on the 1:1 line. *ρc* measures
395 both precision and accuracy. It ranges from -1 to +1 similar to Pearson's correlation coefficient, with
396 perfect agreement at +1 (Lin, 1989; Liao and Lewis, 2000; Akoglu, 2018). Percentage bias (*PBIAS*)
397 measures the average relative difference between observed and estimated values, with an optimal
398 value of 0 (Gupta et al., 1999). Additionally, we evaluate STEEP's model structure by extracting
399 model's performance metrics after excluding it from its main implementations individually (Table 2)
400 and by two-by-two combinations of *z0m*, *rah* and *rλET*. We run the control version of the SEB model,
401 i.e. SEBAL in our case, while incorporating one or two improvements in the model and keeping the
402 remaining parts of the algorithm the same as the reference SEB model.

403 Table 5. Performance metrics used to evaluate ET and *H* in this study.

Performance metric	Equation	Range (Perfect value)
Root mean square error (*RMSE*)	$RMSE = \sqrt{\frac{\sum_{i=1}^{N}(M_i - O_i)^2}{N}}$	[0, +∞ [(0)
Coefficient of determination (R^2)	$R^2 = \frac{\left[\sum_{i=1}^{N}(O_i - \bar{O})(M_i - \bar{M})\right]^2}{\sum_{i=1}^{N}(O_i - \bar{O})^2 \cdot \sum_{i=1}^{N}(M_i - \bar{M})^2}$	[0, 1] (1)
Nash–Sutcliffe efficiency (*NSE*)	$NSE = 1 - \frac{\sum_{i=1}^{N}(M_i - O_i)^2}{\sum_{i=1}^{N}(O_i - \bar{O})^2}$	]-∞, 1] (1)
Concordance correlation coefficient (*ρc*)	$\rho c = \frac{2\sum_{i=1}^{N}(O_i - \bar{O})(M_i - \bar{M})}{\sum_{i=1}^{N}(O_i - \bar{O})^2 + \sum_{i=1}^{N}(M_i - \bar{M})^2 + (N-1)(\bar{O} - \bar{M})^2}$	[-1, 1] (1)
Percentage bias (*PBIAS*)	$PBIAS = \frac{\sum_{i=1}^{N}(M_i - O_i) \cdot 100}{\sum_{i=1}^{N} O_i}$	]-∞, +∞ [(0)

404 where: *N* sample size; O observed value; M modelled value; $\bar{O}$ observed mean; $\bar{M}$ modelled mean.

405 **3. Results and discussion**

406 3.1 Comparison of STEEP and SEBAL models results with observed (EC) values

The performance statistics of daily ET by STEEP and SEBAL in wet and dry seasons for the evaluated sites are shown in Fig. 2. In general, STEEP exhibited a better performance than SEBAL. Although the better statistical metrics of STEEP were in the dry season, in the wet season, they were also superior compared to SEBAL. Specifically, in the dry season, STEEP exhibited a *RMSE* between 0.6 to 1.06 mm/day, while SEBAL was 1.06 to 2.24 mm/day. The maximum value of R^2 in STEEP was 0.62 (sites PTN and SNN), whereas SEBAL achieved only 0.33. The *NSE* metric was the worst among the five analysed in SEBAL: values lower than -7.5 occurred in three of the five sites. Although in STEEP, PTN and SNN sites had values higher than 0 (0.55 and 0.25, respectively) the other sites also had negative values, reaching up to -2.5. In terms of *ρc*, values ranged from 0.09 to 0.77 in STEEP and from -0.04 to 0.41 in SEBAL. It is also possible to see the reduction that STEEP has brought to ET modelling in terms of *PBIAS* when compared to SEBAL.

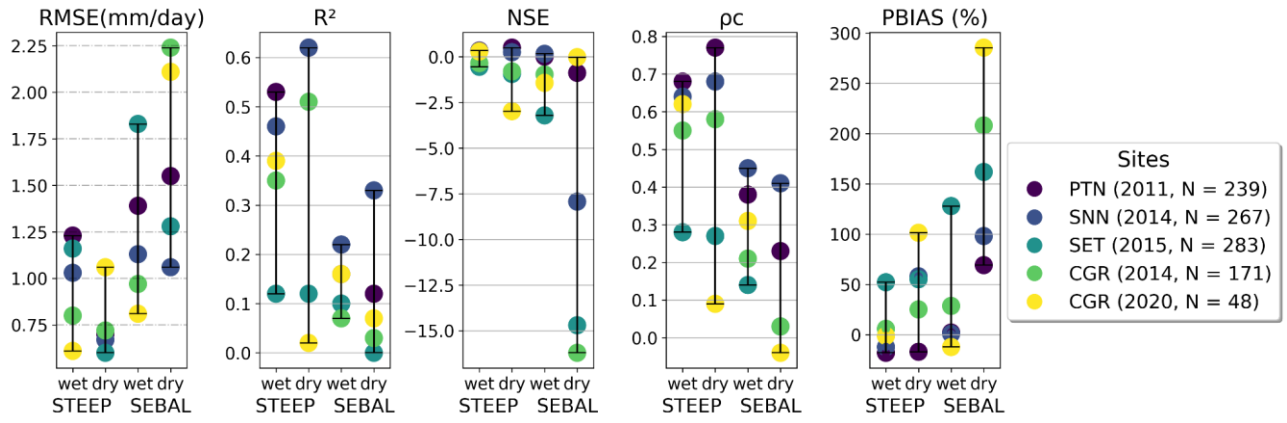

Figure 2. Results of the performance statistics of daily ET in wet and dry seasons for evaluated sites.

Globally, without discriminating between wet and dry seasons, STEEP exhibited better statistical performance than SEBAL at all the evaluated sites (Fig. 3). While STEEP exhibited a *RMSE* between 0.75 and 0.94 mm/day, the *RMSE* for SEBAL was between 1.08 and 1.75 mm/day. In terms of R^2, the values were between 0.24 to 0.69 for STEEP, and were below 0.2 for SEBAL for all sites except in SNN (0.55). Similarly, *NSE* and *ρc* values were higher for STEEP compared to SEBAL. For STEEP, all sites had *NSE* and *ρc* values above -0.42 and 0.41, respectively, whereas all sites except SNN had values below these limits for SEBAL. Both models overestimated ET

(*PBIAS* > 0), with the exception of the STEEP estimates for the PTN site. The highest overestimation by the STEEP model was less than 60%, whereas in SEBAL it was greater than 140%.

SEBAL metrics concerning the modelled ET were similar to those found in other studies. Laipelt et al. (2021) found R^2 ranging from 0.18 to 0.87 when applying SEBAL and comparing it with data from ten EC towers located in different Brazilian biomes (Amazon, Cerrado, Pantanal, and Pampa). Cheng et al. (2021) obtained R^2 of 0.53–0.77 and *RMSE* of 0.89–1.02 mm/day when comparing estimates from SEBAL and EC towers on different land covers in China. Costa et al. (2021), when applying SEBAL in the Caatinga, found R^2 and *NSE* values of 0.57 and 0.36, respectively. Santos et al. (2020) modelled ET with SEBAL at the SNN site for the 2014–2016 period and obtained R^2 and *RMSE* values of 0.28 and 1.43 mm/day, respectively. For this site, we obtained R^2 and *RMSE* of 0.55 and 1.08 mm/day, respectively, for the year 2014 using SEBAL.

STEEP exhibited a greater seasonal accuracy compared to SEBAL (Fig. 3), as evidenced by the goodness-of-fit between simulated and observed values expressed by the *NSE* indicator. STEEP estimates followed the same temporal evolution as the observed values. STEEP satisfactorily captured both minimum and maximum ET values, including after rainfall events, this is particularly evident in Fig. 3a, where the two observed ET peaks in late 2011 — between DOY 300 and 360 — in the PTN site were captured nicely by STEEP. This improved performance can be explained because soil moisture is incorporated in the STEEP algorithm. In semi-arid regions and particularly in the SDTF, besides the availability of energy, evapotranspiration is highly dependent on the soil–water availability (Lima et al., 2012; Carvalho et al., 2018; Mutti et al., 2019; Paloschi et al., 2020). In rainy months, low daily ET rates are often observed due to the reduced levels of incoming radiation caused by high cloud cover (Mutti et al., 2019; Paloschi et al., 2020). Towards the end of the wet period, when the available energy increases, the daily ET values also increase as a result of the high soil water availability from previous precipitation events (Allen et al., 2011; Marques et al., 2020). In the transition period from the rainy to the dry season, the leaves do not fall immediately (see Table 1, main tree species). Instead, leaf-shedding depends on the environmental conditions in each location, including the rainy season duration, and species composition (Lima and Rodal, 2010; Lima et al., 2012; Miranda et al., 2020; Paloschi et al., 2020; Queiroz et al., 2020; Medeiros et al., 2022). The remaining water available in the soil or previously accumulated in plant tissues is sufficient for

458 the Caatinga vegetation to maintain its leaves, for short periods, at levels similar to the rainy season
459 (Barbosa et al., 2006; Mutti et al., 2019). However, in the dry season, when soil moisture reaches its
460 lowest levels, the Caatinga vegetation enters a state of dormancy that is accompanied by leaf drop
461 and a drastic reduction of photosynthetic activity (and hence of transpiration) as a strategy to cope
462 with the lack of available soil moisture (Dombroski et al., 2011; Paloschi et al., 2020). This resilience
463 mechanism is typical of xerophytic and/or deciduous species such as those found in the Caatinga
464 (Lima et al., 2012; Mutti et al., 2019; Paloschi et al., 2020), and explains the low rates of ET in the
465 dry season. In contrast, in SEBAL, which does not consider water availability, it was observed that
466 the daily ET followed the course of the daily net radiation throughout the year, especially in the dry
467 period of each of the experimental sites. This is in agreement with the results of Kayser et al. (2022),
468 who pointed out that estimates with SEBAL can be seasonally accurate in locations where the main
469 driver of ET is the available energy. Our results highlight that SEB models such as SEBAL, which
470 are formulated to be mainly dependent on energy availability and do not consider soil and plant water
471 availability, may not satisfactorily represent ET in semi-arid vegetation such as that found in the
472 SDTF (Gokmen et al., 2012; Paul et al., 2014; Melo et al., 2021).

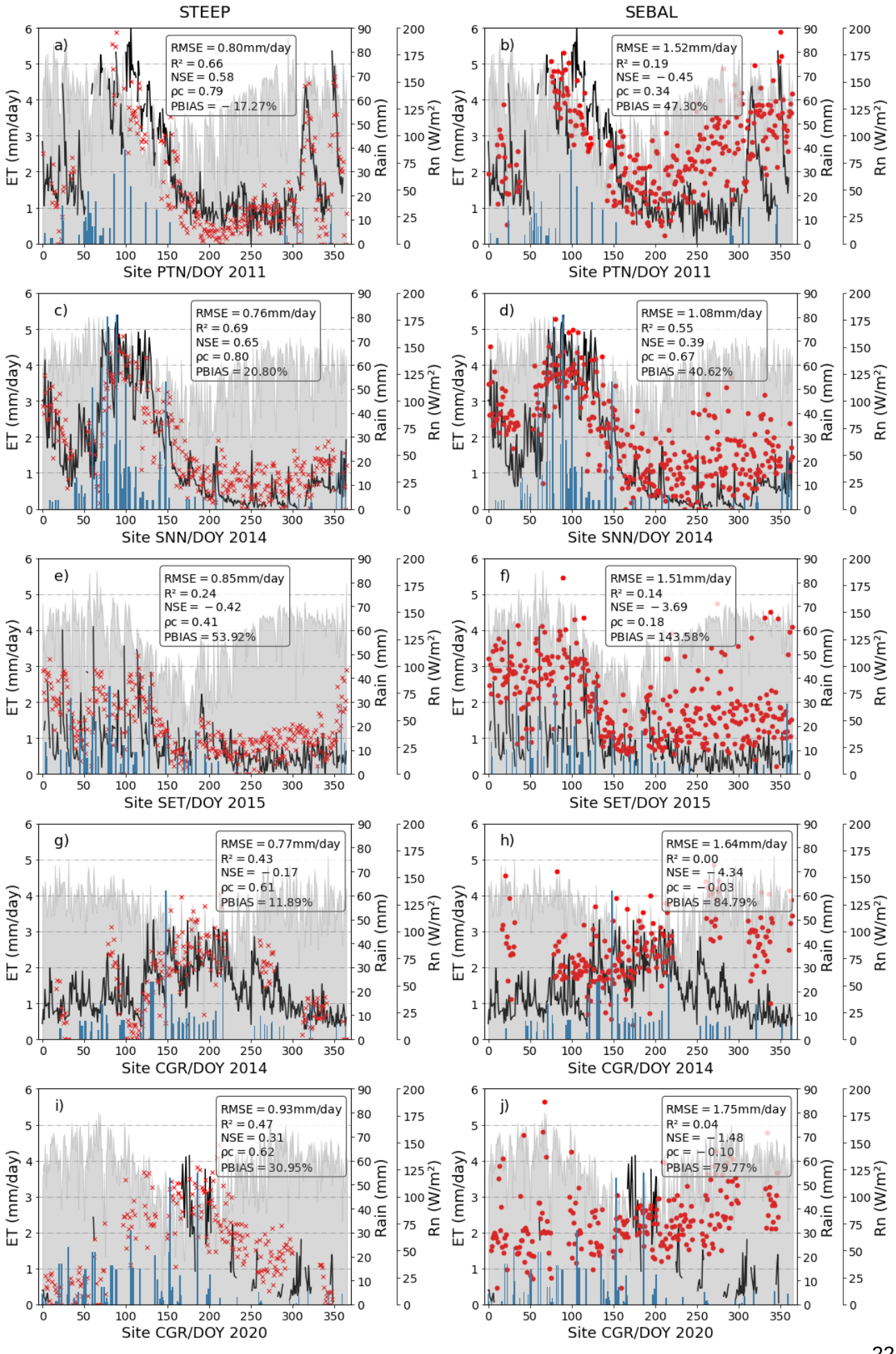
STEEP
SEBAL
a)
RMSE = 0.80mm/day
R² = 0.66
NSE = 0.58
ρc = 0.79
PBIAS = −17.27%
Site PTN/DOY 2011
b)
RMSE = 1.52mm/day
R² = 0.19
NSE = −0.45
ρc = 0.34
PBIAS = 47.30%
Site PTN/DOY 2011
c)
RMSE = 0.76mm/day
R² = 0.69
NSE = 0.65
ρc = 0.80
PBIAS = 20.80%
Site SNN/DOY 2014
d)
RMSE = 1.08mm/day
R² = 0.55
NSE = 0.39
ρc = 0.67
PBIAS = 40.62%
Site SNN/DOY 2014
e)
RMSE = 0.85mm/day
R² = 0.24
NSE = −0.42
ρc = 0.41
PBIAS = 53.92%
Site SET/DOY 2015
f)
RMSE = 1.51mm/day
R² = 0.14
NSE = −3.69
ρc = 0.18
PBIAS = 143.58%
Site SET/DOY 2015
g)
RMSE = 0.77mm/day
R² = 0.43
NSE = −0.17
ρc = 0.61
PBIAS = 11.89%
Site CGR/DOY 2014
h)
RMSE = 1.64mm/day
R² = 0.00
NSE = −4.34
ρc = −0.03
PBIAS = 84.79%
Site CGR/DOY 2014
i)
RMSE = 0.93mm/day
R² = 0.47
NSE = 0.31
ρc = 0.62
PBIAS = 30.95%
Site CGR/DOY 2020
j)
RMSE = 1.75mm/day
R² = 0.04
NSE = −1.48
ρc = −0.10
PBIAS = 79.77%
Site CGR/DOY 2020
ET (mm/day)
Rain (mm)
Rn (W/m²)
Observed ET
STEEP
SEBAL
RAIN - CHIRPS
Daily net radiation

473

Figure 3. Observed and modelled daily evapotranspiration (ET, mm/day) for the different experimental sites: a) and b) PTN 2011, c) and d) SNN 2014, e) and f) SET 2015, g) and h) CGR 2014, i) and j) CGR 2020. The black lines represent observed ET; the red crosses and points are STEEP and SEBAL estimates, respectively; the blue bars represent CHIRPS daily rainfall; the gray region represents daily net radiation from ERA5-land.

The core of the STEEP and SEBAL algorithms is based on finding λET as the residual of the energy balance; however, they differ with regards to the approach used to calculate H. In the STEEP model, the seasonal variation of H fitted the observed values of the instantaneous measurements at 11:00 am (local time) better than SEBAL, for all the sites (Fig. 4). Our results show that an improvement in H leads to a correspondent in ET estimates. This is contrary to the findings of Faivre et al. (2017), who used the same formulation for kB^{-1} applied in our study, but included four different methods to compute z0m. While STEEP estimates of H exhibited ρc values over 0.5 for three of the five sites, SEBAL H estimates exhibited ρc values below 0.5 for all sites. When wet and dry seasons data are analysed separately (Fig. 5), the same trend is observed in the results: in general, the STEEP model presents better statistical metrics than SEBAL.

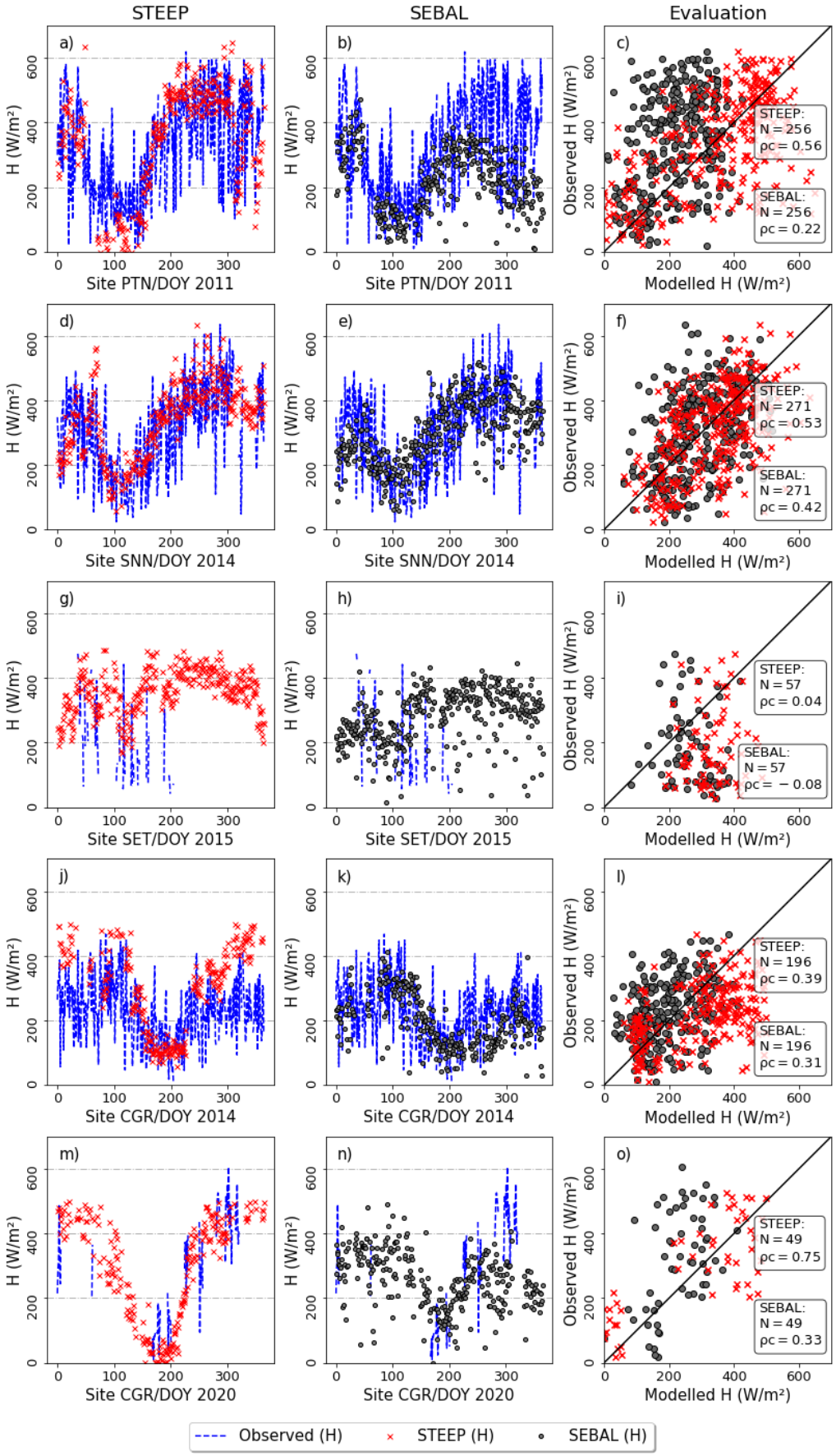

Figure 4. Observed and modelled instantaneous sensible heat flux (*H*, at 11:00 am, W/m^2) for the different experimental sites: a), b) and c) PTN 2011, d), e) and f) SNN 2014, g), h) and i) SET

2015, j), k) and l) CGR 2014, m), n) and o) CGR 2020. The blue line represents the observed values; the red crosses and grey points correspond to the STEEP and SEBAL estimates, respectively. The black line is the 1:1 line.

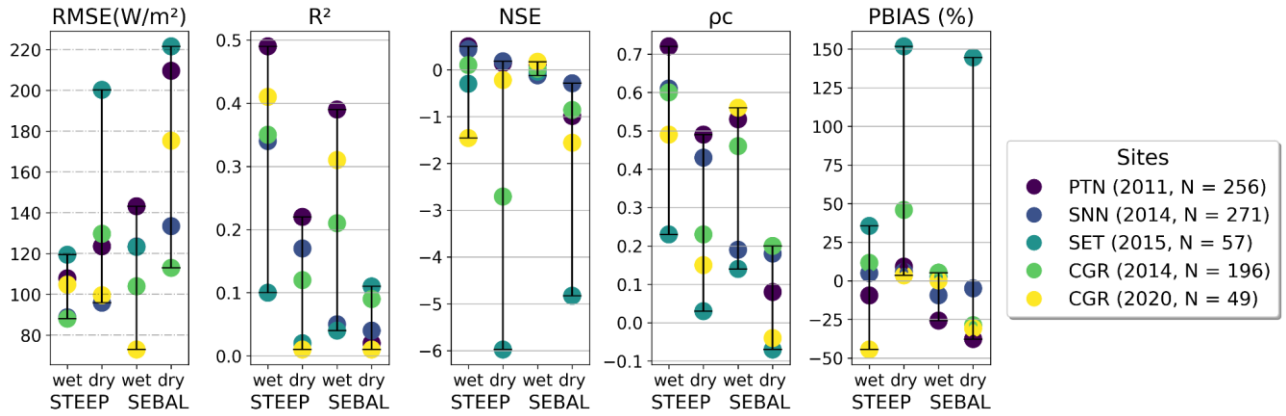

Figure 5. Results of the performance statistics of instantaneous sensible heat flux (*H*, at 11:00 am, W/m^2) in wet and dry seasons, for the evaluated sites.

Evaluation of the STEEP and SEBAL daily ET and instantaneous *H* for all experimental sites (Fig. 6) indicates that both models lack a high performance for *H* estimates, although the use of STEEP resulted in better statistical measures than when SEBAL was employed (Fig. 6b). This substantiates previous findings (Gokmen et al., 2012; Paul et al., 2014; Trebs et al., 2021), that have shown the tendency of underestimation (overestimation) of H (ET) at water-limited sites. It can be seen that the overestimation of *H* by the STEEP model, compared to SEBAL, produced modelled ET values that were closer to the EC measurements (see Fig. 3 and 4).

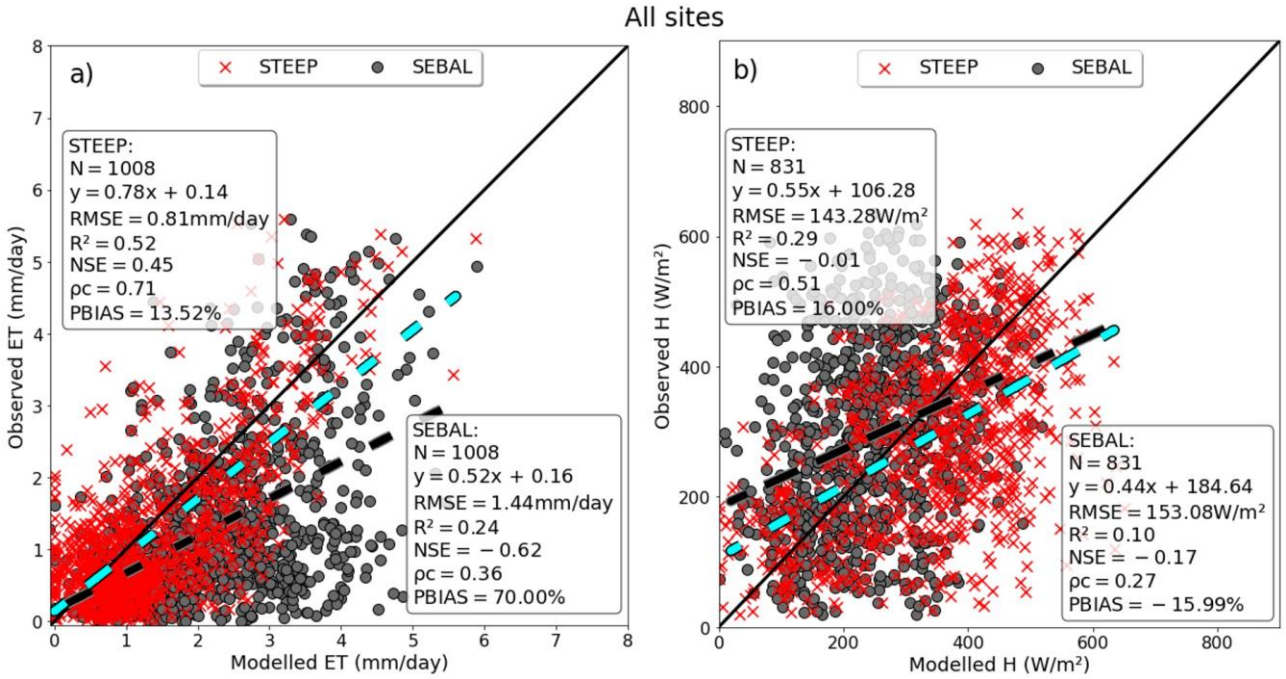

Figure 6. Evaluation of observed and modelled: (a) daily evapotranspiration (ET, mm/day) and b) instantaneous sensible heat flux (*H*, at 11:00 am, W/m^2) for all experimental sites. STEEP (red crosses) and SEBAL (black points). The black line is the 1:1 line; the cyan (black) dashed line is the fitted linear regression between observed and STEEP (SEBAL) model values.

We attribute the better performance of STEEP over SEBAL for the Brazilian Caatinga to at least three reasons, shown in order of impact of model implementation on its performance (Fig. 7 and Table S1). First, by quantifying the remaining *λET* in the endmembers pixels through the Priestley-Taylor equation, a more reliable estimate of *H* in the endmembers pixels can be obtained, as was also evidenced by Singh and Irmak (2011). This process is critical for the subsequent numerical calculation of *H* in SEB models that use *dT*, as its accuracy is closely related to quantifying the energy balance at the hot and cold endmembers (Trezza, 2006; Allen et al., 2007; Singh and Irmak, 2011; Singh et al., 2012). Secondly, roughness characteristics near the surface where the heat fluxes originate are parameterised by *z0m*, which depends on several factors, such as wind direction, height and type of the vegetation cover (Kustas et al., 1989b). Estimation of *z0m* only with an exponential relationship, as a function of vegetation indices, may be an oversimplification (Kustas et al., 1989a; Paul et al., 2013). In our study, *z0m* and *d0* are calculated with the equations and coefficients proposed in Raupach (1994) and Verhoef et al. (1997b), and using PAI because this

index better represents the intra-annual phenological changes in the Caatinga (Miranda et al., 2020). This procedure considers the characteristics of SDTF, such as seasonality of phenology and vegetation height, that considerably affect the quantification of turbulent transfer (Liu et al., 2021). Third, our study uses the equation described in Verhoef et al. (1997a) and Paul et al. (2013) to estimate *rah*, which considers the differences between heat and momentum transfer, unlike the original equation employed in other SEB models e.g. SEBAL or METRIC that only considers *z0m* and sets *z0h* = 0.1 when computing this resistance. Furthermore, we account for the kB^{-1} parameter that varies in space and time and incorporates the soil moisture content obtained by RS (Su et al., 2001; Gokmen et al., 2012). ET estimation is best represented with a spatially varying kB^{-1} values, as pointed out by the studies of Gokmen et al. (2012) and Paul et al. (2014). Long et al. (2011) report that the introduction of these fixed values (*z0h* or kB^{-1}) has a significant impact on the magnitudes of the estimates of H. Furthermore, Mallick et al. (2018) and Trebs et al. (2021) indicate that the parameterization of rah can influence the estimation of ET, especially in SEB models that are largely dependent on *rah*. Our results show that including just one or two of the refinements had only partial performance gains (Fig. 7 and Table S1). In contrast, all the proposed STEEP improvements when implemented together resulted in the best performance metrics for all sites.

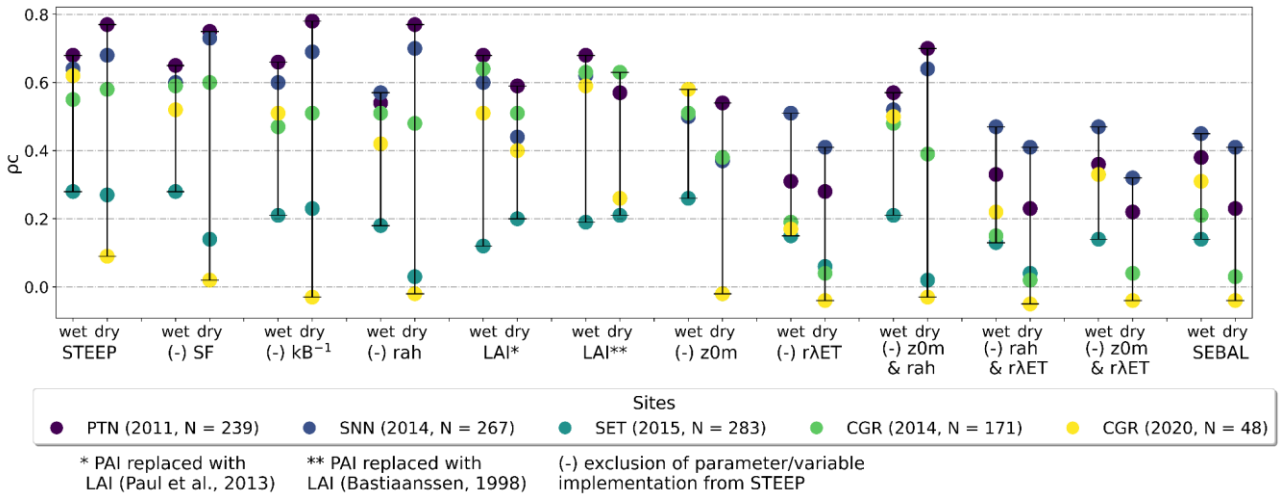

Figure 7. Change of the concordance correlation coefficient (ρc) by the exclusion/modification of one or two parameters/variables implemented in the STEEP model, in the wet and dry seasons: scale factor soil moisture correction (SF), the parameter kB^{-1}, the aerodynamic resistance for heat transfer (rah), PAI replace with LAI (determined by two different methods), the roughness length for momentum transport (z0m) and the residual latent heat flux in the end members pixels (*rλET*).

3.2 Comparison of STEEP model estimates with global evapotranspiration products

The comparison of ET estimates by STEEP, MOD16 and PMLv2 with the observed values at the different sites (Fig. 8) reveals that the ET estimates by STEEP and global products adequately followed the seasonality of the values, with a better fit for STEEP and MOD16. In general, the evaluation at the different sites shows that the *RMSE* of STEEP was not higher than 6.45 mm/8 days, while the ET products' maximum *RMSE* was close to 15 mm/8 days. It is noted that the lowest *RMSE* value found (4.11 mm/8 days) was for MOD16 at the SET site. Regarding R^2 values, 80% of the evaluations with STEEP were equal to or greater than 0.50. For MOD16, 60% of the R^2 values were equal to or greater than 0.70, while for PMLv2, no site had R^2 values that exceeded 0.55. The best *NSE* value produced by STEEP was 0.77, while with MOD16, it was 0.70, both at the SNN site, while PMLv2 did not exceed 0.39 (PTN site). Regarding ρc, the percentages of ET evaluations that obtained values equal to or greater than 0.70 were 60% for STEEP and MOD16, and only 20% for PMLv2 (site PTN). The overestimations (*PBIAS*) with STEEP were not higher than 50%, and not higher than 95% with MOD16. For PMLv2 the overestimations did not exceed 80%, except for the SET site that obtained a *PBIAS* approx. 160%.. We highlight the good performance of MOD16 for the SET, SNN, and especially the PTN sites, with very good performance metrics and seasonal behaviour, capturing ET values in dry periods very well. The evaluation results of STEEP, MOD16 and PMLv2 for all observation sites combined are shown in Fig. 9. Noteworthy is the better performance of STEEP over MOD16 and PMLv2, with *RMSE* < 6 mm/8 days, R^2 and *NSE* greater than or close to 0.60, ρc > 0.75 and an average overestimation < 12%. Analysis with the dataset considering only the 8-day time periods without missing field-observed data, i.e. periods with valid ET measurements during eight consecutive days (Fig. S3) did not change the results overall, confirming STEEP's dominance compared to the two standard products evaluated.

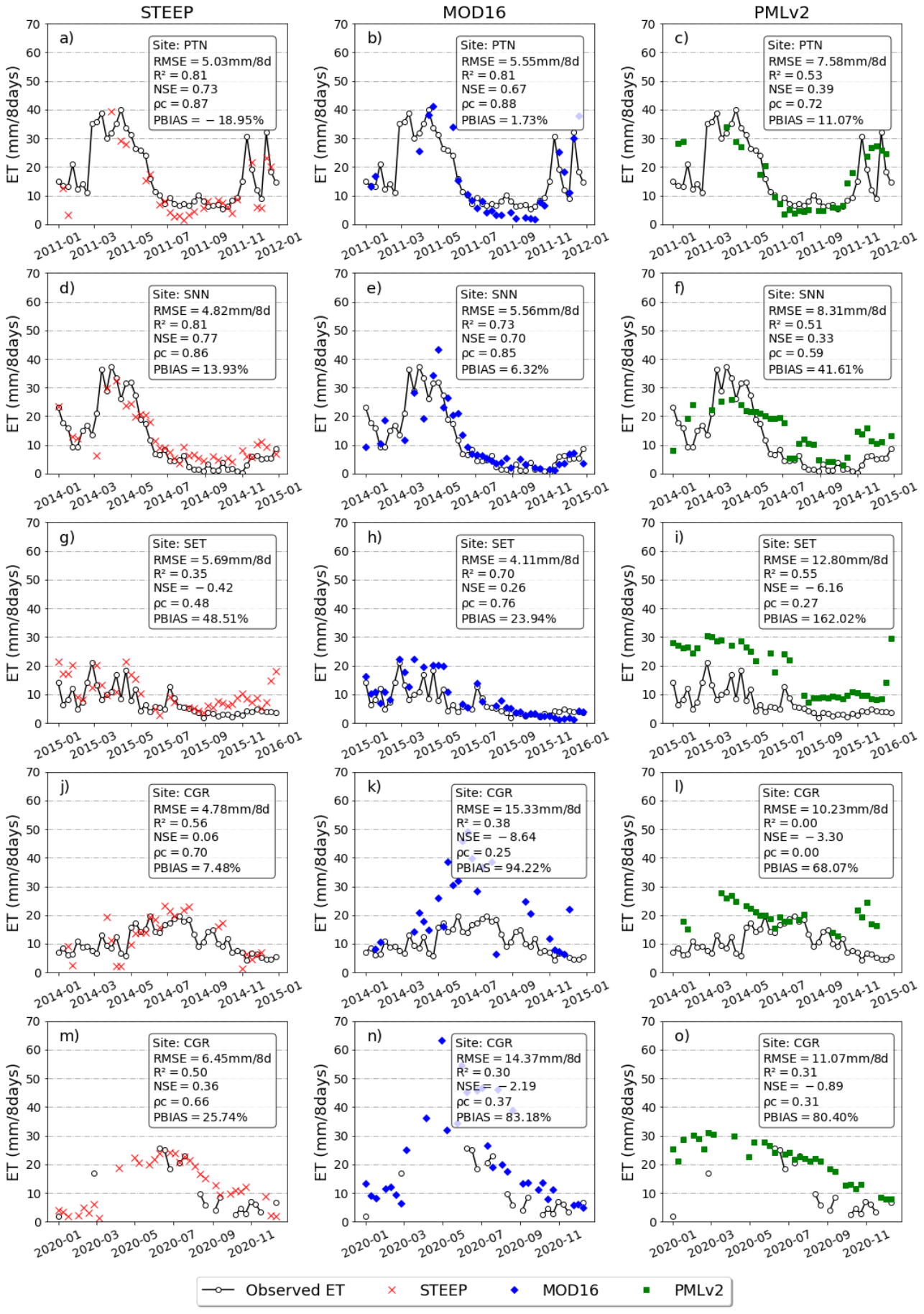
STEEP
MOD16
PMLv2
a)
Site: PTN
RMSE = 5.03mm/8d
R² = 0.81
NSE = 0.73
ρc = 0.87
PBIAS = − 18.95%
b)
Site: PTN
RMSE = 5.55mm/8d
R² = 0.81
NSE = 0.67
ρc = 0.88
PBIAS = 1.73%
c)
Site: PTN
RMSE = 7.58mm/8d
R² = 0.53
NSE = 0.39
ρc = 0.72
PBIAS = 11.07%
d)
Site: SNN
RMSE = 4.82mm/8d
R² = 0.81
NSE = 0.77
ρc = 0.86
PBIAS = 13.93%
e)
Site: SNN
RMSE = 5.56mm/8d
R² = 0.73
NSE = 0.70
ρc = 0.85
PBIAS = 6.32%
f)
Site: SNN
RMSE = 8.31mm/8d
R² = 0.51
NSE = 0.33
ρc = 0.59
PBIAS = 41.61%
g)
Site: SET
RMSE = 5.69mm/8d
R² = 0.35
NSE = − 0.42
ρc = 0.48
PBIAS = 48.51%
h)
Site: SET
RMSE = 4.11mm/8d
R² = 0.70
NSE = 0.26
ρc = 0.76
PBIAS = 23.94%
i)
Site: SET
RMSE = 12.80mm/8d
R² = 0.55
NSE = − 6.16
ρc = 0.27
PBIAS = 162.02%
j)
Site: CGR
RMSE = 4.78mm/8d
R² = 0.56
NSE = 0.06
ρc = 0.70
PBIAS = 7.48%
k)
Site: CGR
RMSE = 15.33mm/8d
R² = 0.38
NSE = − 8.64
ρc = 0.25
PBIAS = 94.22%
l)
Site: CGR
RMSE = 10.23mm/8d
R² = 0.00
NSE = − 3.30
ρc = 0.00
PBIAS = 68.07%
m)
Site: CGR
RMSE = 6.45mm/8d
R² = 0.50
NSE = 0.36
ρc = 0.66
PBIAS = 25.74%
n)
Site: CGR
RMSE = 14.37mm/8d
R² = 0.30
NSE = − 2.19
ρc = 0.37
PBIAS = 83.18%
o)
Site: CGR
RMSE = 11.07mm/8d
R² = 0.31
NSE = − 0.89
ρc = 0.31
PBIAS = 80.40%
ET (mm/8days)
Observed ET
STEEP
MOD16
PMLv2

571

Figure 8. Temporal evolution of ET from STEEP, MOD16 and PMLv2 for the different observation sites, and their individual performance statistics. a), b) and c) PTN 2011; d), e) and f) SNN 2014; g) h) and i) SET 2015; j), k) and l) CGR 2014; m), n) and o) CGR 2020. Black lines correspond to observed ET while data points refer to estimates by the STEEP model (red crosses), MOD16 (blue diamonds) and PMLv2 (green squares) products.

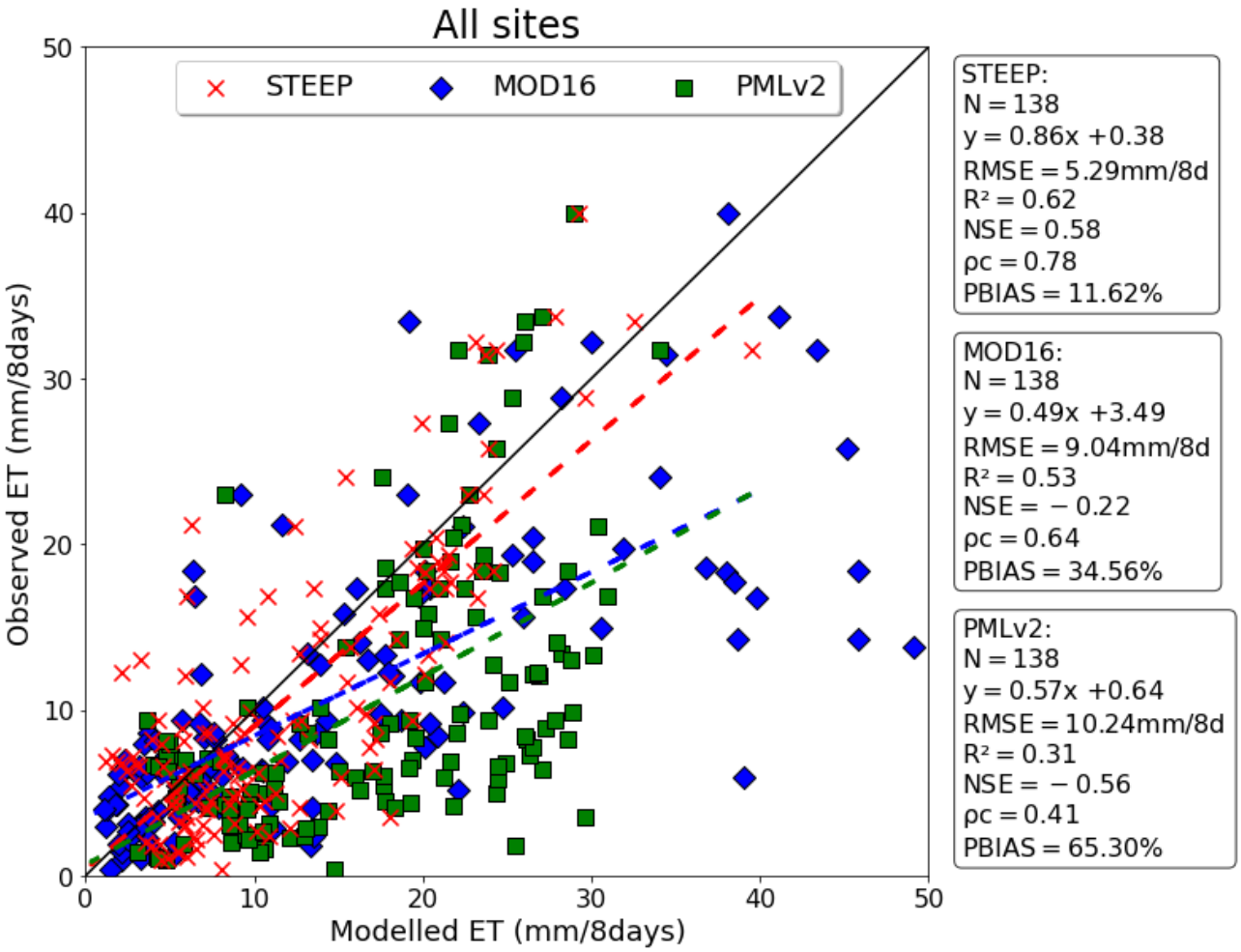

Figure 9. Evaluation of evapotranspiration (ET, mm/8 days) observed and modelled with STEEP (red crosses), MOD16 (blue diamonds) and PMLv2 (green squares) for all experimental sites. The black line is the 1:1 line; dashed lines are the fitted linear regressions of observed versus modelled values by the STEEP model (red), MOD16 (blue) and PMLv2 (green) products. N = 138 is the total number of eight-day periods with at least one day of EC data measured in at least one of the five experimental sites of Caatinga where all the ET models (STEEP, MOD16 and PMLv2) outputs were available.

585 The explanation of the differences between STEEP and the MOD16 and PMLv2 products is
586 two-fold. Firstly, the way ET is obtained differs between STEEP and the other products. While
587 STEEP and other SEB single-source models estimate ET as a combined single process, i.e. soil
588 evaporation and transpiration estimates are provided as a lumped sum (Sahnoun et al., 2021), and
589 interception loss is not taken into account, MOD16 and PMLv2 discriminate the ET components, i.e.
590 soil evaporation, transpiration, and wet canopy evaporation (Mu et al., 2011; Zhang et al., 2019).
591 With this in mind it is remarkable that STEEP performs better than the other, widely used, multiple-
592 source ET products. Secondly, the input data sets and their uses are different. The driving
593 meteorological data for STEEP are from ERA5-Land, while in MOD16, they are from MERRA and in
594 PMLv2 are provided by GLDAS (Mu et al., 2011; Zhang et al., 2019). In addition, the meteorological
595 elements used are different among the ET products. MOD16 requires air temperature, atmospheric
596 pressure, relative humidity, and downward shortwave radiation. In addition to these elements,
597 PMLv2 also requires precipitation, downward longwave radiation, and wind speed (Mu et al., 2011;
598 Zhang et al., 2019; Yin et al., 2020; Chen et al., 2022). Although both ET products use the same
599 land cover data (MOD12Q1), only MOD16 integrates it into its algorithm. In MOD16, the land cover
600 type defines biome delimitation for the characterization of leaf stomatal conductance, vapour
601 pressure deficit (VPD) and other related factors, while PMLv2 only uses land cover to construct a
602 mask of the land area (Chen et al., 2022). The sources and use of LAI in these two products are also
603 different. LAI is used to increase leaf conductance in MOD16, while it is used to divide the total
604 available energy into canopy uptake and soil uptake in PMLv2 (Mu et al., 2011; Zhang et al., 2019;
605 Chen et al., 2022). Although MOD16 uses EC data from 46 distributed sites for validation (Mu et al.,
606 2011) and PMLv2 uses EC data from 95 distributed sites and ten plant functional types for calibration
607 (Zhang et al., 2019; Yin et al., 2020), none of the products had observation sites in SDTF.
608 The uncertainties associated with field measurements of ET can also influence the evaluation
609 of the model products. It is generally accepted that EC flux towers provide reliable local, i.e. for areas
610 of relatively limited spatial extensions, ca. 10 km², ET measurements (Mu et al., 2011; Chu et al.,
611 2021; Salazar-Martínez et al., 2022). However, generally flux tower data have a lack of energy
612 balance closure, that is the difference between net radiation and ground heat flux is sometimes
613 greater than the sum of the turbulent latent and sensible heat fluxes, an error that can be in the range

of 10–30% (Wilson et al., 2002; Foken, 2008; Allen et al., 2011). This gap can result from instrument errors, weather and surface conditions, e.g. those that result in advection, and gap-filling methods (Mu et al., 2011). In addition, the complex and heterogeneous canopy structure, the stochastic nature of turbulence (Hollinger and Richardson, 2005) and adverse weather conditions, e.g. rainy and stormy days, tower sensors recording abnormal values, can affect ET measurements obtained by EC systems (Ramoelo et al., 2014).

3.3 Sources of error and further research for STEEP

In its current configuration, STEEP has some limitations that should be noted. Meteorological reanalysis provides only large-scale averages and can misrepresent local meteorological conditions; hence, it suffers from biases, especially over heterogeneous surfaces (Rasp et al., 2018). However, despite moderate accuracy and biases at regional scales, ground-based assimilation and reanalysis data have become important sources of meteorological inputs for ET estimates (Mu et al., 2011; Zhang et al., 2019; Allam et al., 2021; Senay et al., 2022). Laipelt et al. (2020) and Kayser et al. (2022) showed that global reanalysis data when used as meteorological inputs had modest effects only on the accuracy of SEBAL for estimating ET. In our study, ERA5-Land exhibited relatively high and satisfactory agreement with micrometeorological data measured at each site (Fig S4). Also, although gap-filling was used in the present study to improve the availability of LST data, this procedure should be used with caution. In addition, care should be taken when using the MCD43A4 reflectance product, because in its composition there is also gap-filling. For example, on some cloudy days, the estimates of vegetation indices, surface albedo and LST may have introduced inaccuracies in the STEEP (and in SEBAL) model calculation process due to these gap-filling methods. Regarding the selection of endmembers pixels, although the temporal evolution of the selected pixels in this study seems plausible, their representativeness of the actual conditions may be debatable, especially considering the considerable extent of the AOI. The computational capacity and the effectiveness of GEE for running SEB models should be commended. Although other studies have demonstrated GEE's strength (Laipelt et al., 2021; Jaafar et al., 2022; Senay et al., 2022), this platform has some limitations when it comes to the number of iterations, e.g. a convergence threshold cannot be set to stop the within-loop iterations of *H* calculations; instead a fixed number of

iterations needs to be defined. Still, the availability of the several necessary datasets within one platform greatly facilitates the run of STEEP and other SEB models.

One of the main focuses of this study is to provide a one-source model capable of representing ET in environments that are mainly governed by soil–water availability, such as those represented by SDTF, in a parsimonious way. Based on our findings we deem this main aim to be achieved due to the relative simplicity of the STEEP model and its low data demand. The improved performance of STEEP was the result of improvement of existing and physically meaningful parameters (*z0m* and kB^{-1}), rather than by introducing additional empirical parameters, thereby satisfying the principle of equifinality (see Beven and Freer, 2001). To explore further the potential and accuracy of STEEP, more research is needed to analyse the impact that the improved *H* approach has on ET of different land covers at longer time scales. Improving the quantification of regional ET via RS-based SEB models has a great potential to provide a more accurate estimate of the energy and water fluxes in SDTF regions, and will contribute to a better understanding of the water cycle, its uses, and the interrelationships with ecosystem functioning.

4. Conclusions

Our work developed a calibration-free model (STEEP) with an improved approach for estimating the latent and sensible heat fluxes by remote sensing for SDTF. In summary, the main conclusions are:

- The estimates of *H* by STEEP allowed ET estimates to be closer to the observed field values than those obtained by SEBAL. Based on all the performance metrics used to analyse the models, STEEP was superior to SEBAL. STEEP showed *RMSE* less than 1mm/day, R^2 between 0.24 and 0.69, *NSE* between -0.17 and 0.65, ρc between 0.41 and 0.80 and *PBIAS* between -17% to 54%. Also noteworthy is how well STEEP captured the seasonal course of observed ET.
- Compared with ET data from the global MOD16 and PMLv2 products, the STEEP model simulated a similar but generally superior seasonal evolution and its performance metrics were also better. Considering all observation sites simultaneously, at the eight-day scale, STEEP showed superior performance with *RMSE* less than 6 mm/8 days, R^2 and *NSE* equal to or greater than 0.60, ρc greater than 0.75, and an overestimation of < 12%.

Thus, we conclude that STEEP, a one-source model that incorporated the seasonality of the aerodynamic and surface variables, was well-heeled in representing ET in environments that are mainly governed by soil–water availability. All the same, there is a need to evaluate the newly developed STEEP model performance for different land covers, climate, and for longer time series than those considered during the modelling process in this study.

Acknowledgements

The Coordenação de Aperfeiçoamento de Pessoal de Nível Superior-Brazil (CAPES)-Finance Code 001, provided scholarships to the first and fifth authors. This work was funded by the Brazilian National Council for Scientific and Technological Development (CNPq), grant 409341/2021-5, by the Paraiba Scientific Foundation (FAPESQ), under startup grant 010/2021, and by São Paulo Scientific Foundation (FAPESP), grant 2015/24461-2. CEF is a research unit funded by Fundação para a Ciência e a Tecnologia I.P. (FCT), Portugal (UIDB/00239/2020). RLBN and AV acknowledge support by the Newton/NERC/FAPESP Nordeste project (NE/N012526/1 ICL 652 and NE/N012488/1 UoR). RLBN acknowledges support from the European Research Council under the European Union's Horizon 2020 research and innovation programme (grant agreement No: 787203 REALM).

Data Availability Statement

ET data for the PTN, SNN, and SET sites were published by Melo et al. (2021), and are available at https://doi.org/10.5281/zenodo.5549321. ET data for the CGR site; H data for the PTN, SNN, CGR sites, and the code used for the formulation of the STEEP model presented in this study can be accessed at https://doi.org/10.5281/zenodo.7109043 and https://github.com/ulissesaalencar/ET_SDTF, respectively. H data for the SET site is publicly available for download at https://ameriflux.lbl.gov/.

Supplementary material

Table S1. Performance statistics by the exclusion/modification of one or two parameters/variables implemented in the STEEP model, in the wet and dry seasons: scale factor soil moisture correction (SF), the parameter kB^{-1}, the aerodynamic resistance for heat transfer (rah), PAI replace with LAI (determined by two different methods), the roughness length for momentum transport (z0m), the residual latent heat flux in the end members pixels ($r\lambda ET$), and of the SEBAL model.

699

Site		Performance statistics									
		RMSE		*R^2*		*NSE*		*ρ_c*		*PBIAS*	
		wet	*dry*	*wet*	*dry*	*wet*	*dry*	*wet*	*dry*	*wet*	*dry*
PTN (N = 239; 2011)	STEEP	1.23	0.7	0.53	0.62	0.34	0.5	0.68	0.77	-18.01	-17.01
	(-) SF	1.38	0.69	0.56	0.58	0.16	0.52	0.65	0.75	-26.39	-7.99
	(-) kB-1	1.39	0.67	0.54	0.62	0.14	0.55	0.66	0.78	-23.37	-8.23
	(-) rah	1.61	0.66	0.42	0.6	-0.22	0.55	0.54	0.77	-32.42	-6.56
	*LAI**	1.37	1.08	0.57	0.59	0.19	-0.18	0.68	0.59	-24.24	-56.26
	*LAI***	1.27	0.91	0.54	0.34	0.28	0.17	0.68	0.57	-19.73	-11.95
	(-) z0m	1.48	0.88	0.36	0.3	0.01	0.21	0.5	0.54	-25.94	7.55
	(-) rλET	1.5	1.6	0.12	0.19	-0.15	-1.54	0.31	0.28	14.75	75.96
	(-) z0m & rah	1.51	0.72	0.44	0.51	-0.04	0.48	0.57	0.7	-28.85	4.4
	(-)rah & rλET	1.47	1.66	0.13	0.15	-0.11	-1.81	0.33	0.23	12.99	81.63
	(-) z0m & rλET	1.42	1.45	0.14	0.09	-0.31	-0.04	0.36	0.22	0.73	57.29
	SEBAL	1.39	1.55	0.16	0.12	0.01	-1.43	0.38	0.23	2.12	69.2
SNN (N = 267; 2014)	STEEP	1.03	0.6	0.46	0.62	0.32	0.25	0.64	0.68	-12.17	58.08
	(-) SF	1.07	0.58	0.47	0.64	0.29	0.44	0.6	0.73	-17.2	42.77
	(-) kB-1	1.12	0.67	0.44	0.59	0.21	0.24	0.6	0.69	-17.86	50.26
	(-) rah	1.19	0.6	0.49	0.62	0.19	0.41	0.57	0.7	-25.47	47.33
	*LAI**	1.38	0.8	0.54	0.3	-0.21	-0.07	0.6	0.44	-29.33	-58.36
	*LAI***	1.19	0.98	0.52	0.09	0.07	-0.6	0.62	0.26	23.77	55.02
	(-) z0m	1.14	0.83	0.41	0.23	0.24	-0.16	0.5	0.37	-19.01	60.45
	(-) rλET	1.16	1.18	0.32	0.43	0.18	-1.33	0.51	0.41	12.96	122.85
	(-) z0m & rah	1.19	0.63	0.52	0.57	0.17	0.34	0.52	0.64	-26.49	50.69
	(-)rah & rλET	1.13	1.14	0.25	0.37	0.16	-1.19	0.47	0.41	6.43	111.65
	(-) z0m & rλET	1.13	1.03	0.24	0.17	0.16	-0.79	0.47	0.32	-5.86	79.17
	SEBAL	1.13	1.06	0.22	0.33	0.16	-0.88	0.45	0.41	0.91	98.12
SET (N = 283; 2015)	STEEP	1.16	0.6	0.12	0.12	-0.55	-0.94	0.28	0.27	52.19	55.18

	(-) SF	1.04	0.61	0.11	0.02	-0.25	-0.99	0.28	0.14	36.58	38.26
	(-) kB-1	1.13	0.58	0.06	0.07	-0.49	-0.86	0.21	0.23	36.71	40.83
	(-) rah	1.06	0.56	0.04	0	-0.43	-1.03	0.18	0.03	21.82	39.71
	*LAI**	1.3	0.68	0.03	0.09	-0.98	-1.51	0.12	0.2	-62.3	-75.32
	*LAI***	1.15	0.6	0.04	0.05	-0.53	-0.97	0.19	0.21	-6.83	-29.78
	(-) z0m	1.09	0.75	0.1	0	-0.36	-2.74	0.26	-0.02	42.62	80.96
	(-) rλET	2.11	1.37	0.15	0.04	-4.18	-9.27	0.15	0.06	151.66	190.07
	(-) z0m & rah	1.06	0.58	0.05	0	-0.3	-1.24	0.21	0.02	21.6	51.96
	(-)rah & rλET	1.99	1.37	0.11	0.01	-3.99	-9.27	0.13	0.04	143.27	183.22
	(-) z0m & rλET	1.66	1.16	0.07	0.01	-2.47	-6.31	0.14	0.04	104.32	134.34
	SEBAL	1.83	1.28	0.1	0	-3.21	-7.93	0.14	0.03	128	161.89
CGR (N = 171; 2014)	STEEP	0.8	0.72	0.35	0.51	-0.35	-0.8	0.55	0.58	5.85	25.16
	(-) SF	0.7	0.67	0.36	0.52	-0.02	-0.53	0.59	0.6	6.57	30.14
	(-) kB-1	0.78	0.8	0.25	0.44	-0.28	-1.18	0.47	0.51	15.04	38.9
	(-) rah	0.71	0.78	0.28	0.46	-0.06	-1.07	0.51	0.48	-8.54	54.63
	*LAI**	0.76	0.83	0.49	0.61	-0.23	-1.35	0.64	0.51	-7.64	-62.39
	*LAI***	0.75	0.68	0.46	0.58	-0.18	-0.57	0.63	0.63	-9.25	-26.31
	(-) z0m	0.71	0.83	0.28	0.35	-0.05	-1.35	0.51	0.38	-11.12	62.72
	(-) rλET	1.15	2.32	0.09	0.07	-1.77	-17.48	0.19	0.04	46.68	217.84
	(-) z0m & rah	0.69	0.84	0.24	0.44	-0.01	-1.43	0.48	0.39	3.9	68.9
	(-)rah & rλET	1.14	2.44	0.05	0.03	-1.72	-19.4	0.15	0.02	43.77	229.58
	(-) z0m & rλET	0.85	1.97	0.11	0.04	-0.51	-12.27	0.33	0.04	9.18	175.39
	SEBAL	0.97	2.24	0.07	0.03	-0.97	-14.7	0.21	0.03	28.63	208.13
CGR (N = 48; 2020)	STEEP	0.61	1.06	0.39	0.02	0.29	-2.98	0.62	0.09	-1.19	101.37
	(-) SF	0.82	1.03	0.3	0	-0.29	-2.76	0.52	0.02	-6.52	106.36
	(-) kB-1	0.83	1.26	0.29	0	-0.3	-4.63	0.51	-0.03	-5.31	135.98
	(-) rah	1.11	1.13	0.25	0	-1.2	-3.55	0.42	-0.02	-15.37	133.29
	*LAI**	0.85	1.02	0.29	0.01	-0.38	-0.99	-3.06	0.4	-4.71	31.63
	*LAI***	0.67	0.76	0.36	0.07	0.14	-1.03	0.59	0.26	-3.58	2.87

(-) z0m	0.69	1.03	0.41	0	0.15	-2.73	0.58	-0.02	-12.29	106.1
(-) rλET	0.99	2.25	0.03	0.06	-0.52	-16.98	0.17	-0.04	6.37	312.54
(-) z0m & rah	1.04	1.13	0.34	0.01	-0.74	-3.52	0.5	-0.03	-16.56	134.92
(-)rah & rλET	0.89	2.38	0.05	0.14	-0.24	-19.08	0.22	-0.05	1.07	330.94
(-) z0m & rλET	0.83	1.77	0.18	0.02	-0.6	-10.14	0.33	-0.04	-14.15	216.81
SEBAL	0.81	2.11	0.16	0.07	-0.02	-0.02	0.31	-0.04	-12.25	285.53

700

701 *z0m* = roughness length for momentum transfer; *rah* = aerodynamic resistance for heat transfer; r*λET* = remaining *λET* in the endmembers pixels.

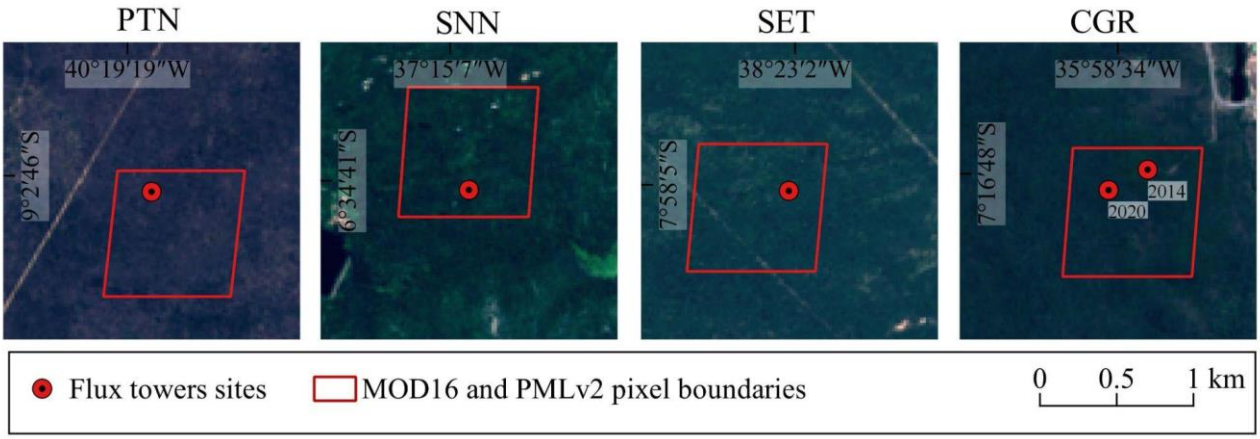

Figure S1. Location of the flux towers sites and MOD16 and PMLv2 pixel boundaries. True colour composite (bands 4, 3, and 2) of Harmonized Sentinel-2 MSI acquired via Google Earth Engine. Scene acquired of PTN (12/06/2021); SNN and SET (25/05/2021); CGR (29/07/2021).

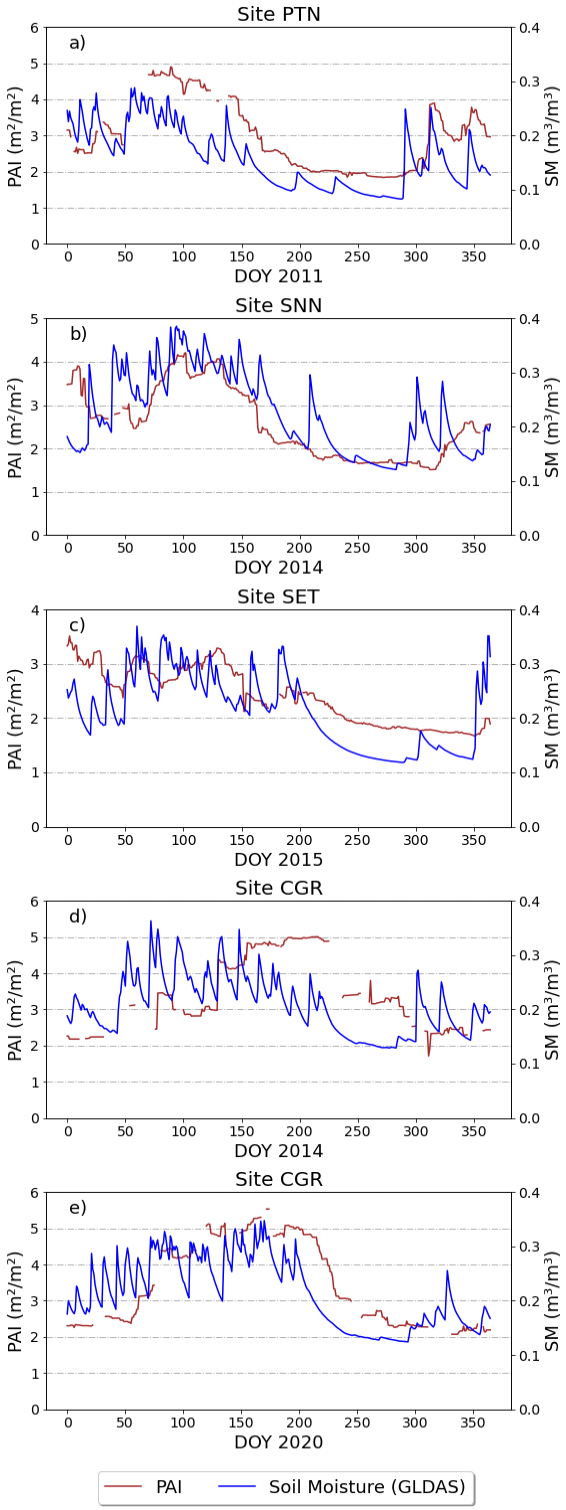

Figure S2. PAI and soil moisture time series for the different observation sites.

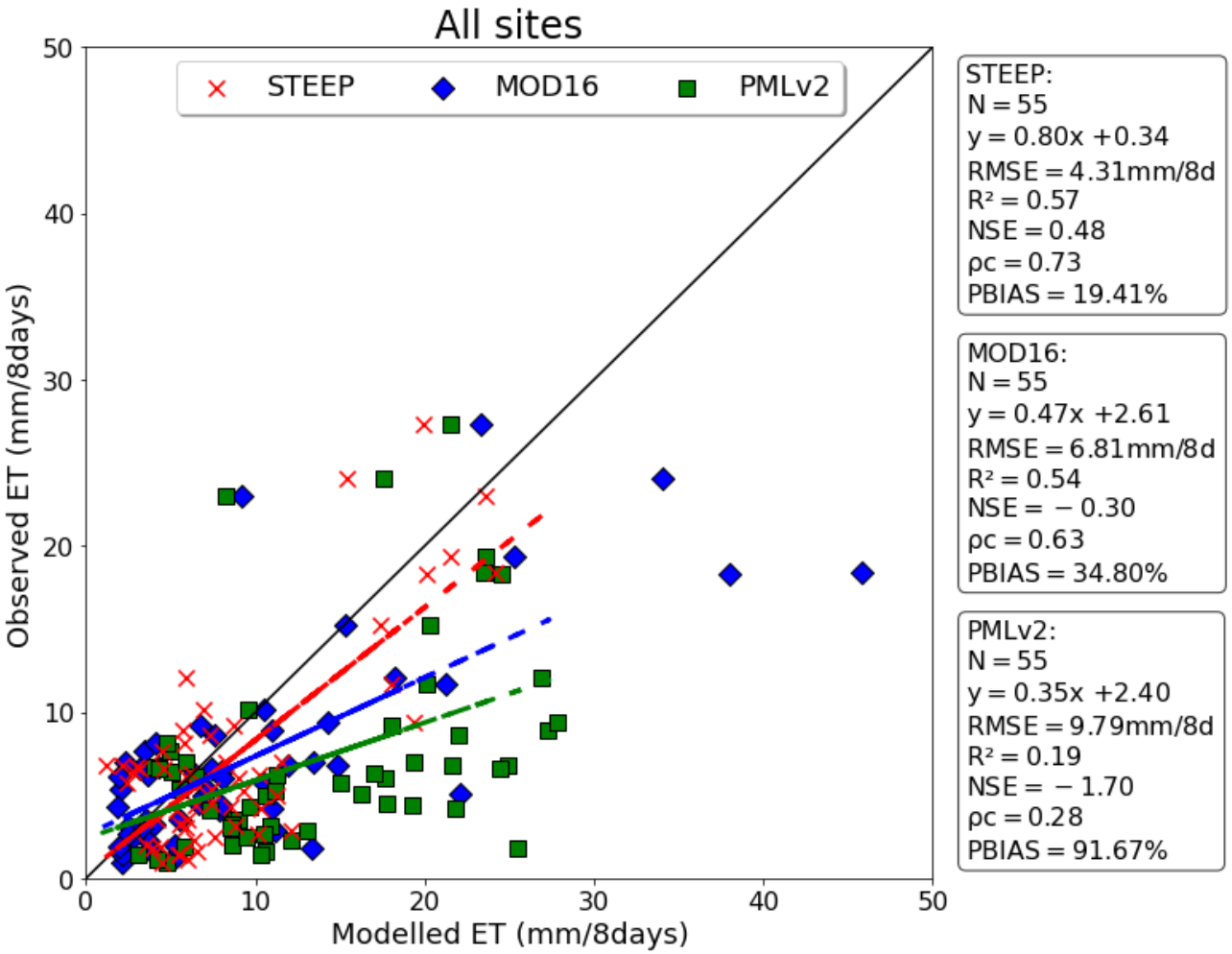

Figure S3. Evaluation of evapotranspiration (ET, mm/8 days) observed and modelled with STEEP (red crosses), MOD16 (blue diamonds) and PMLv2 (green squares) for all experimental sites considering only the 55 periods where the field-observed data had eight consecutive days. The black line is the 1:1 line; dashed lines are the fitted linear regressions of observed or modelled values by the STEEP model (red), MOD16 (blue) and PMLv2 (green) products.

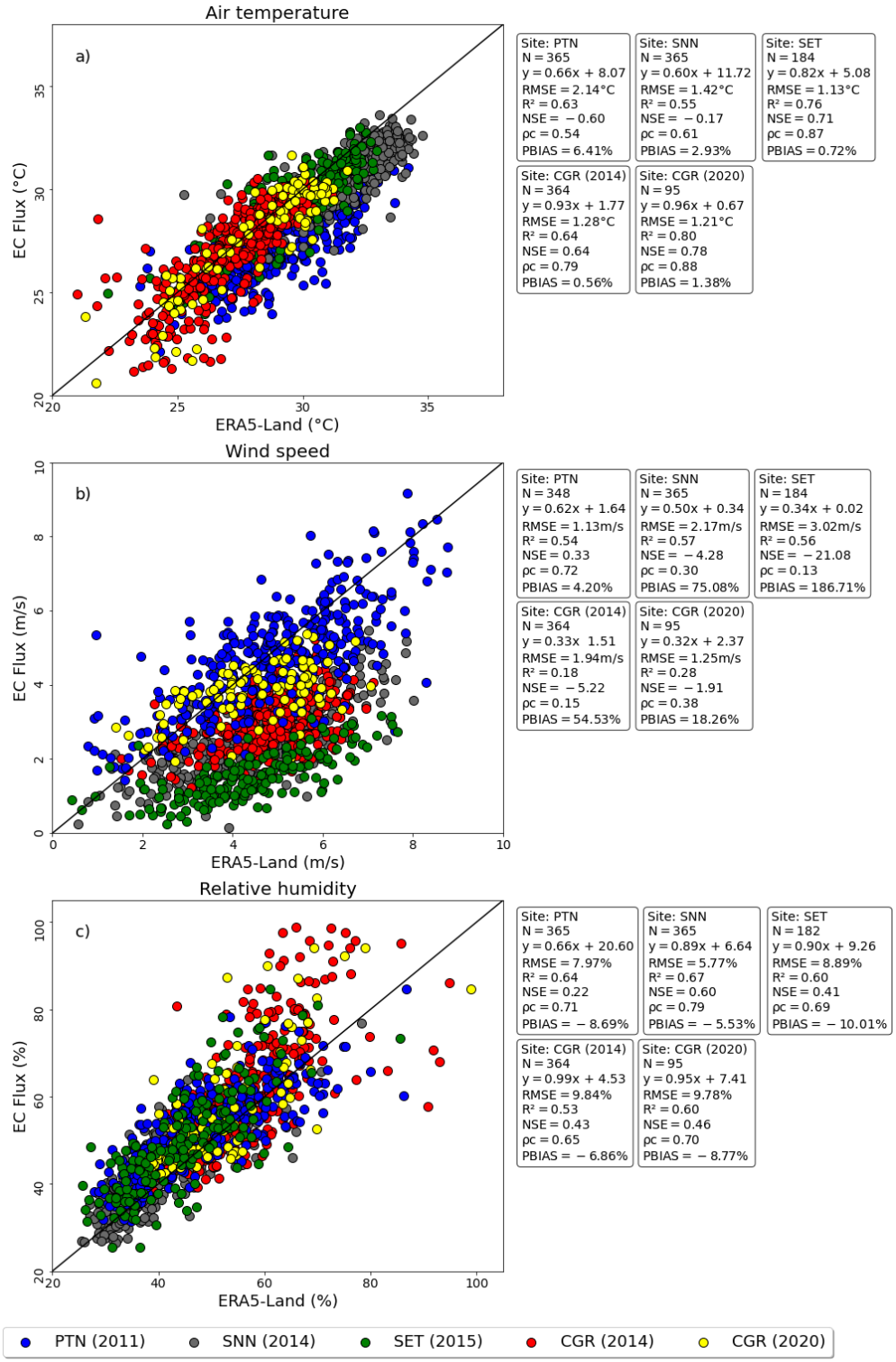

Figure S4. Comparison between ERA5-Land reanalysis dataset and local observational meteorological measurements from the flux tower at the closest time from the satellite overpass. Micrometeorological sensors installed at the flux towers are up to 16 m in distance from the land surface, and ERA5-Land variables have different reference elevation (e.g. 2 m for air temperature and 10 m to wind speed).

Appendix A – Equations adopted to formulate the STEEP model

Latent heat flux (λET) was modeled using Eq. (A.1):

$$\lambda ET = Rn - G - H \quad \text{(A.1)}$$

where R_n is net radiation, G is soil heat flux, and H is sensible heat flux. All variables are expressed in energy units (e.g., W/m^2).

Net radiation (Rn) was modeled based on the radiation budget indicated by Allen et al. (2007) and Ferreira et al. (2020) by Eq. (A.2):

$$Rn = R_{S\downarrow} \times (1 - \alpha) + \varepsilon_S \times R_{L\downarrow} - R_{L\uparrow} \quad \text{(A.2)}$$

where $R_{S\downarrow}$ is incident shortwave radiation (W/m^2) estimated following Allen et al. (2007), α is surface albedo (dimensionless), estimated following Trezza et al. (2013), $R_{L\downarrow}$ is longwave radiation from the atmosphere (W/m^2) estimated following Ferreira et al. (2020) with atmospheric emissivity from Duarte et al. (2006); $R_{L\uparrow}$ is emitted longwave radiation (W/m^2) following Ferreira et al. (2020) with ε_S the surface emissivity (dimensionless), estimated following Long et al. (2010).

Soil heat flux (G), expressed as a ratio of net radiation, was estimated following the model by Bastiaanssen et al. (1998):

$$\frac{G}{Rn} = [(LST - 273.15) \times (0.0038 + 0.0074 \times \alpha) \times (1 - 0.98 \times NDVI^4)] \quad \text{(A.3)}$$

where *LST* is the surface temperature (K) and NDVI is the Normalized Difference Vegetation Index (dimensionless), estimated following Rouse et al. (1973).

Sensible heat flux (H) was modeled using:

$$H = \frac{\rho \times c_p \times dT}{rah} \quad \text{(A.4)}$$

where ρ is the air density (kg/m^3), c_p refers to the specific heat of air at constant pressure (J/kg/K), *dT* is the temperature gradient (K), and *rah* is the aerodynamic resistance for heat transfer (s/m).

Aerodynamic resistance to heat transport was estimated based on the classical equation given in Paul et al. (2013), see also Verhoef et al. (1997a):

$$rah = \frac{1}{k \times u^*} \times \left[ln\left(\frac{z_{ref} - d0}{z0m}\right) - \psi_h \right] + \frac{1}{k \times u^*} \times kB_{umd}^{-1} \quad \text{(A.5)}$$

where k is the von Kármán constant taken as 0.41, u^* is the friction velocity (m/s), z_{ref} is the reference height (m), *d0* is zero plane displacement height (m), *z0m* is roughness length for momentum transfer (m), ψ_h is the atmospheric stability correction function for heat transfer (m), as calculated following Paulson (1970), kB_{umd}^{-1} is the dimensionless parameter formulated to express the excess resistance of heat transfer compared to momentum transfer, corrected for soil moisture derived from remote sensing.

The friction velocity was computed according to Verhoef et al. (1997b) and Paul et al. (2013):

$$u^* = k \times u \left[ln\left(\frac{z_{ref} - d0}{z0m}\right) - \psi_m \right]^{-1} \quad \text{(A.6)}$$

where u is the wind speed (m/s) at a known height z_{ref}, ψ_m is the atmospheric stability correction function for momentum transfer (m), as calculated following Paulson (1970).

Roughness length for momentum transport was estimated, based on the studies by Verhoef et al. (1997b):

$$z0m = (HGHT - d0) \times exp^{(-k \times \gamma + PSICORR)} \quad \text{(A.7)}$$

where $HGHT$ is the height of the vegetation (m), $PSICORR$ is taken as 0.2 and γ is the inverse of the square root of the bulk surface drag coefficient at the roughness canopy height (Raupach, 1992).

Zero plane displacement height ($d0$) was obtained following Raupach (1994) from:

$$d0 = HGHT \times \left[\left(1 - \frac{1}{\sqrt{CD1 \times PAI}}\right) + \left(\frac{exp^{-\sqrt{CD1 \times PAI}}}{\sqrt{CD1 \times PAI}}\right) \right] \quad \text{(A.8)}$$

where $CD1$ is taken as 20.6 and *PAI* is the Plant Area Index.

γ was following Verhoef et al. (1997b):

$$\gamma = \left(CD + CR \times \frac{PAI}{2}\right)^{-0.5} \quad \text{(A.9)}$$

if γ < 3.33, γ is set to 3.33. Following Verhoef et al. (1997), CD and CR are taken as 0.01 and 0.35, respectively.

Plant Area Index was calculated according to Miranda et al. (2020) as:

$$PAI = 10.1 \times \left(\rho_{NIR} - \sqrt{\rho_{RED}}\right) + 3.1 \quad \text{(A.10)}$$

where ρ_{NIR} is the near infrared band reflectance, and ρ_{RED} is the red band reflectance. If *PAI* < 0, *d0* is set to 0.

The dimensionless parameter kB_{umd}^{-1} is corrected by soil moisture by remote sensing following the equations provided by Gokmen et al. (2012):

$$kB_{umd}^{-1} = SF \times kB^{-1} \quad \text{(A.11)}$$

where *SF* is a scaling factor, represented by a sigmoid function:

$$SF = \left[c + \frac{1}{1 + exp^{(d - e \times SM_{rel})}}\right] \quad \text{(A.12)}$$

Here, c, d, e are the sigmoid function coefficients, for which we adopted values of 0.3, 2.5, and 4, respectively, following Gokmen et al. (2012). SM_{rel} is the relative soil moisture, obtained from:

$$SM_{rel} = \frac{SM - SM_{min}}{SM_{max} - SM_{min}} \quad \text{(A.13)}$$

where SM is the actual soil moisture content, in our case obtained with the GLDAS reanalysis product, and SM_{min} and SM_{max} are the minimum and maximum soil moisture. The SM_{min} and SM_{max} values were obtained using the annual time series analysis of the soil moisture data.

kB^{-1} was calculated according to Su et al. (2001):

$$kB^{-1} = \frac{k \times Cd}{4 \times Ct \times \frac{u^*}{u(h)} \times \left(1 - exp^{\left(-\frac{nec}{2}\right)}\right)} \times f_c^2 + \frac{k \times \frac{u^*}{u(h)} \times \frac{z0m}{h}}{C_t^*} \times f_c^2 \times f_s^2 + kBs^{-1} \times f_s^2 \quad \text{(A.14)}$$

where $kBs^{-1} = 2.46(Re^*)^{0.25} - 2$, Cd is the drag coefficient of the foliage elements taken as 0.2, Ct is the heat transfer coefficient of the leaf with value 0.01.

The ratio $\frac{u^*}{u(h)}$ is parameterized as:

$$\frac{u^*}{u(h)} = c1 - c2 \times exp^{(-c3 \times Cd \times PAI)} \quad \text{(A.15)}$$

where $c1$ = 0.320, $c2$ = 0.264, $c3$ = 15.1.

nec is the extinction coefficient of the wind speed profile within the canopy given by:

$$nec = \frac{Cd \times PAI}{\frac{2u^{*2}}{u(h)^2}} \quad \text{(A.16)}$$

779 C_t^* is heat transfer coefficient of the soil given by:

$$C_t^* = Pr^{-2/3} \times (Re)^{-1/2} \quad \text{(A.17)}$$

780 where Pr is the Prandtl number with a value 0.71, and Re is the Reynolds number calculated as:

$$Re = \frac{u^* \times 0.009}{v}, \qquad v = 1.461 \times 10^{-5} \quad \text{(A.18)}$$

781 where v is the kinematic viscosity (m^2/s).

782 In Eq. A.14 f_c is the fractional canopy cover calculated according to Eq. (A19), and f_s is its
783 complement.

$$f_c = 1 - \left[\frac{NDVI - NDVI_{max}}{NDVI_{min} - NDVI_{max}}\right]^{0.4631} \quad \text{(A.19)}$$

784 where $NDVI_{max}$ and $NDVI_{min}$ are maximum and minimum NDVI values, respectively. $NDVI_{max}$ and
785 $NDVI_{min}$ values were obtained using the annual time series analysis of the NDVI.

786 *dT* in Eq. (A4) was estimated daily with a linear relationship on the surface temperature
787 (Bastiaanssen et al., 1998) as:

$$dT = a + b \times LST \quad \text{(A.20)}$$

788 To find the coefficients a and b in Eq. (A20) requires that hot and cold endmembers pixels are
789 established. The coefficients were found as:

$$b = \frac{(dT_{hot} - dT_{cold})}{(LST_{hot} - LST_{cold})} \quad \text{(A.21)}$$

$$a = dT_{cold} - b \times LST_{cold} \quad \text{(A.22)}$$

$$dT_{hot/cold} = \frac{H_{hot/cold} \times rah_{hot/cold}}{\rho \times c_p} \quad \text{(A.23)}$$

$$H_{hot/cold} = Rn_{hot/cold} - G_{hot/cold} - \lambda ET_{hot/cold} \quad \text{(A.24)}$$

where $dT_{hot/cold}$ are dT values for the hot/dry and cold/wet endmember pixels, respectively, $Rn_{hot/cold}$, $G_{hot/cold}$, $LST_{hot/cold}$, $rah_{hot/cold}$ are the median values extracted on the endmember pixels of each variable. The selection of endmember pixels is detailed in section 2.3.

$\lambda ET_{hot/cold}$ is the term incorporated in the computation of *H* in the endmember pixels given by the Priestley-Taylor (1972) equation, according to Singh and Irmak (2011) and French et al. (2015):

$$\lambda ET_{hot/cold} = \left(Rn_{hot/cold} - G_{hot/cold}\right) \times f_c \times \alpha pt \times \left[\frac{\Delta}{\Delta + \gamma_c}\right] \quad \text{(A.25)}$$

where αpt is the empirical Priestley-Taylor coefficient, nominally set to 1.26, but here adjusted according to local conditions, i.e. we adopted the αpt values (0.55 for hot/dry and 1.75 for cold/wet pixels) based on Ai and Yang (2016). Δ is the slope of the saturation vapor pressure-air temperature curve (kPa/ºC) and γ_c is the psychrometric constant (kPa/ºC).

The actual daily evapotranspiration (mm/day) was obtained by means of the following relationship:

$$ET_{24h} = \frac{86400}{(2.501 - 0.00236 \times T_a) \times 10^6} \times \frac{\lambda ET}{Rn - G} \times Rn_{24h} \quad \text{(A.26)}$$

where T_a is the mean daily air temperature (°C), *λET* is derived from Eq. A1, and Rn_{24h} corresponds to the daily net radiation (W/m^2); in this study both driving variables were obtained with data from the ERA5-Land product.

References

Ai, Z., & Yang, Y. (2016). Modification and Validation of Priestley–Taylor Model for Estimating Cotton Evapotranspiration under Plastic Mulch Condition. Journal of Hydrometeorology, 17(4), 1281–1293. doi:10.1175/jhm-d-15-0151.1

Akoglu, H. (2018). User's guide to correlation coefficients. Turkish Journal of Emergency Medicine, 18(3), 91-93. doi: 10.1016/j.tjem.2018.08.001

Alberton, B., Torres, R. da S., Cancian, L. F., Borges, B. D., Almeida, J., Mariano, G. C., … Morellato, L. P. C. (2017). Introducing digital cameras to monitor plant phenology in the tropics: applications for conservation. Perspectives in Ecology and Conservation, 15(2), 82–90. doi:10.1016/j.pecon.2017.06.004

Allam, M., Mhawej, M., Meng, Q., Faour, G., Abunnasr, Y., Fadel, A., & Xinli, H. (2021). Monthly 10-m evapotranspiration rates retrieved by SEBALI with Sentinel-2 and MODIS LST data. Agricultural Water Management, 243, 106432. doi:10.1016/j.agwat.2020.106432

Allen, R. G., Tasumi, M., & Trezza, R. (2007). Satellite-Based Energy Balance for Mapping Evapotranspiration with Internalized Calibration (METRIC)—Model. Journal of Irrigation and Drainage Engineering, 133(4), 380–394. doi:10.1061/(asce)0733-9437(2007)133:4(380)

Allen, K., Dupuy, J. M., Gei, M. G., Hulshof, C., Medvigy, D., Pizano, C., … Powers, J. S. (2017). Will seasonally dry tropical forests be sensitive or resistant to future changes in rainfall regimes? Environmental Research Letters, 12(2), 023001. doi:10.1088/1748-9326/aa5968

Allen, R. G., Pereira, L. S., Howell, T. A., & Jensen, M. E. (2011). Evapotranspiration information reporting: I. Factors governing measurement accuracy. Agricultural Water Management, 98(6), 899–920. doi:10.1016/j.agwat.2010.12.015

Alvares, C. A., Stape, J. L., Sentelhas, P. C., Gonçalves, J. D. M., & Sparovek, G. (2013). Köppen's climate classification map for Brazil. Meteorologische Zeitschrift, 22(6), 711-728. doi:10.1127/0941-2948/2013/0507

Anapalli, S. S., Ahuja, L. R., Gowda, P. H., Ma, L., Marek, G., Evett, S. R., & Howell, T. A. (2016). Simulation of crop evapotranspiration and crop coefficients with data in weighing lysimeters. Agricultural Water Management, 177, 274–283. doi:10.1016/j.agwat.2016.08.009

Anderson, M. C., Kustas, W. P., Norman, J. M., Hain, C. R., Mecikalski, J. R., Schultz, L., … Gao, F. (2011). Mapping daily evapotranspiration at field to continental scales using geostationary and polar orbiting satellite imagery. Hydrology and Earth System Sciences, 15(1), 223–239. doi:10.5194/hess-15-223-2011

Andrade, J., Cunha, J., Silva, J., Rufino, I., & Galvão, C. (2021). Evaluating single and multi-date Landsat classifications of land-cover in a seasonally dry tropical forest. Remote Sensing Applications: Society and Environment, 22, 100515. doi:10.1016/j.rsase.2021.100515

838 Antonino, A. C. D. (2019), AmeriFlux BASE BR-CST Caatinga Serra Talhada, Ver. 1-5, AmeriFlux
839 AMP, (Dataset). https://doi.org/10.17190/AMF/1562386

840 Araújo, J. C., & González Piedra, J. I. (2009). Comparative hydrology: analysis of a semiarid and a
841 humid tropical watershed. Hydrological Processes, 23(8), 1169–1178. doi:10.1002/hyp.7232

842 Barbosa, H. A., Huete, A. R., & Baethgen, W. E. (2006). A 20-year study of NDVI variability over the
843 Northeast Region of Brazil. Journal of Arid Environments, 67(2), 288–307.
844 doi:10.1016/j.jaridenv.2006.02.022

845 Barbosa, A. D. S., Andrade, A. P. de, Félix, L. P., Aquino, Í. D. S., & Silva, J. H. C. S. (2020).
846 Composição, similaridade e estrutura do componente arbustivo-arbóreo de áreas de Caatinga.
847 Nativa, 8(3), 314–322. doi:10.31413/nativa.v8i3.9494

848 Barraza, V., Restrepo-Coupe, N., Huete, A., Grings, F., Beringer, J., Cleverly, J., & Eamus, D.
849 (2017). Estimation of latent heat flux over savannah vegetation across the North Australian Tropical
850 Transect from multiple sensors and global meteorological data. Agricultural and Forest Meteorology,
851 232, 689-703. doi:10.1016/j.agrformet.2016.10.013

852 Bastiaanssen, W. G. M. (1995). Regionalization of surface flux densities and moisture indicators in
853 composite terrain: A remote sensing approach under clear skies in Mediterranean climates.
854 Wageningen University and Research.

855 Bastiaanssen, W. G. M., Menenti, M., Feddes, R. A., & Holtslag, A. A. M. (1998). A remote sensing
856 surface energy balance algorithm for land (SEBAL). 1. Formulation. Journal of Hydrology, 212-213,
857 198–212. doi:10.1016/s0022-1694(98)00253-4

858 Bastiaanssen, W. G. M., Ahmad, M.-D., & Chemin, Y. (2002). Satellite surveillance of evaporative
859 depletion across the Indus Basin. Water Resources Research, 38(12), 9–1–9–9.
860 doi:10.1029/2001wr000386

861 Bastiaanssen, W. G. M., Noordman, E. J. M., Pelgrum, H., Davids, G., Thoreson, B. P., & Allen, R.
862 G. (2005). SEBAL Model with remotely sensed data to improve water-resources management under

863 actual field conditions. Journal of Irrigation and Drainage Engineering, 131(1), 85–93.
864 doi:10.1061/(asce)0733-9437(2005)131:1(85)

865 Beven, K., & Freer, J. (2001). Equifinality, data assimilation, and uncertainty estimation in
866 mechanistic modelling of complex environmental systems using the GLUE methodology. Journal of
867 Hydrology, 249(1–4), 11–29. doi:10.1016/s0022-1694(01)00421-8

868 Bhattarai, N., Quackenbush, L. J., Im, J., & Shaw, S. B. (2017). A new optimized algorithm for
869 automating endmember pixel selection in the SEBAL and METRIC models. Remote Sensing of
870 Environment, 196, 178–192. doi:10.1016/j.rse.2017.05.009.

871 Bonan, G. B., Patton, E. G., Finnigan, J. J., Baldocchi, D. D., & Harman, I. N. (2021). Moving beyond
872 the incorrect but useful paradigm: reevaluating big-leaf and multilayer plant canopies to model
873 biosphere-atmosphere fluxes – a review. Agricultural and Forest Meteorology, 306, 108435.
874 https://doi.org/10.1016/j.agrformet.2021.108435

875 Borges, C. K., dos Santos, C. A. C., Carneiro, R. G., da Silva, L. L., de Oliveira, G., Mariano, D., …
876 de S. Medeiros, S. (2020). Seasonal variation of surface radiation and energy balances over two
877 contrasting areas of the seasonally dry tropical forest (Caatinga) in the Brazilian semi-arid.
878 Environmental Monitoring and Assessment, 192(8). doi:10.1007/s10661-020-08484-y

879 Brazil, Ministério do Meio Ambiente. Caatinga. https://antigo.mma.gov.br/biomas/caatinga.html.
880 Acessed: 25 March 2021.

881 Cabral, O. M. R., Freitas, H. C., Cuadra, S. V., de Andrade, C. A., Ramos, N. P., Grutzmacher, P.,
882 … Rossi, P. (2020). The sustainability of a sugarcane plantation in Brazil assessed by the eddy
883 covariance fluxes of greenhouse gases. Agricultural and Forest Meteorology, 282-283, 107864.
884 doi:10.1016/j.agrformet.2019.107864

885 Campos, S., Mendes, K. R., da Silva, L. L., Mutti, P. R., Medeiros, S. S., Amorim, L. B., … Bezerra,
886 B. G. (2019). Closure and partitioning of the energy balance in a preserved area of a Brazilian

887 seasonally dry tropical forest. Agricultural and Forest Meteorology, 271, 398–412.
888 doi:10.1016/j.agrformet.2019.03.018

889 Carvalho, H. F. D. S., de Moura, M. S., da Silva, T. G., & Rodrigues, C. T. (2018). Controlling factors
890 of 'Caatinga' and sugarcane evapotranspiration in the Sub-middle São Francisco Valley. Revista
891 Brasileira de Engenharia Agrícola e Ambiental, 22, 225-230. doi:10.1590/1807-
892 1929/agriambi.v22n4p225-230

893 Chai, T., & Draxler, R. R. (2014). Root mean square error (*RMSE*) or mean absolute error (MAE)?
894 – Arguments against avoiding *RMSE* in the literature. Geoscientific Model Development, 7(3), 1247–
895 1250. doi:10.5194/gmd-7-1247-2014

896 Chehbouni, A., Seen, D. L., Njoku, E. G., & Monteny, B. M. (1996). Examination of the difference
897 between radiative and aerodynamic surface temperatures over sparsely vegetated surfaces. Remote
898 Sensing of Environment, 58(2), 177-186. doi: 10.1016/S0034-4257(96)00037-5

899 Chen, J. M., & Liu, J. (2020). Evolution of evapotranspiration models using thermal and shortwave
900 remote sensing data. Remote Sensing of Environment, 237, 111594. doi:10.1016/j.rse.2019.111594

901 Chen, H., Gnanamoorthy, P., Chen, Y., Mansaray, L. R., Song, Q., Liao, K., … Sun, C. (2022).
902 Assessment and Inter-Comparison of Multi-Source High Spatial Resolution Evapotranspiration
903 Products over Lancang–Mekong River Basin, Southeast Asia. Remote Sensing, 14(3), 479.
904 doi:10.3390/rs14030479

905 Cheng, M., Jiao, X., Li, B., Yu, X., Shao, M., & Jin, X. (2021). Long time series of daily
906 evapotranspiration in China based on the SEBAL model and multisource images and validation.
907 Earth System Science Data, 13(8), 3995–4017. doi:10.5194/essd-13-3995-2021

908 Chu, H., et al. (2021) Representativeness of Eddy-Covariance flux footprints for areas surrounding
909 AmeriFlux sites." Agricultural and Forest Meteorology 301-302, 108350.
910 doi:org/10.1016/j.agrformet.2021.108350

911 Costa, J. A.; Navarro-Hevia, J., Costa, C. A. G., & de Araújo, J. C. (2021). Temporal dynamics of
912 evapotranspiration in semiarid native forests in Brazil and Spain using remote sensing. Hydrological
913 Processes, 35(3). doi:10.1002/hyp.14070

914 Costa-Filho, E., Chávez, J. L., Zhang, H., & Andales, A. A. (2021). An optimized surface aerodynamic
915 temperature approach to estimate maize sensible heat flux and evapotranspiration. Agricultural and
916 Forest Meteorology, 311, 108683. doi:10.1016/j.agrformet.2021.108683

917 Cunha, J., Nóbrega, R. L. B., Rufino, I., Erasmi, S., Galvão, C., & Valente, F. (2020). Surface albedo
918 as a proxy for land-cover clearing in seasonally dry forests: Evidence from the Brazilian Caatinga.
919 Remote Sensing of Environment, 238, 111250. doi:10.1016/j.rse.2019.111250

920 Danelichen, V. H. de M., Biudes, M. S., Souza, M. C., Machado, N. G., Silva, B. B. da, & Nogueira,
921 J. de S. (2014). Estimation of soil heat flux in a neotropical Wetland region using remote sensing
922 techniques. Revista Brasileira de Meteorologia, 29(4), 469–482. doi:10.1590/0102-778620120568

923 Dombroski, J. L. D., Praxedes, S. C., de Freitas, R. M. O., & Pontes, F. M. (2011). Water relations
924 of Caatinga trees in the dry season. South African Journal of Botany, 77(2), 430–434.
925 doi:10.1016/j.sajb.2010.11.001

926 Duarte, H. F., Dias, N. L., & Maggiotto, S. R. (2006). Assessing daytime downward longwave
927 radiation estimates for clear and cloudy skies in Southern Brazil. Agricultural and Forest
928 Meteorology, 139(3–4), 171–181. doi:10.1016/j.agrformet.2006.06.008

929 Faivre, R., Colin, J., & Menenti, M. (2017). Evaluation of Methods for Aerodynamic Roughness
930 Length Retrieval from Very High-Resolution Imaging LIDAR Observations over the Heihe Basin in
931 China. Remote Sensing, 9(1), 63. doi:10.3390/rs9010063

932 Farr, T. G., Rosen, P. A., Caro, E., Crippen, R., Duren, R., Hensley, S., ... & Alsdorf, D. (2007). The
933 shuttle radar topography mission. Reviews of geophysics, 45(2). doi:10.1029/2005RG000183

934 Ferreira, T. R., Silva, B. B. D., Moura, M. S. B. D., Verhoef, A., & Nóbrega, R. L. B. (2020). The use
935 of remote sensing for reliable estimation of net radiation and its components: a case study for

936 contrasting land covers in an agricultural hotspot of the Brazilian semiarid region. Agricultural and
937 Forest Meteorology, 291, 108052. doi:10.1016/j.agrformet.2020.108052

938 Foken, T. (2008). The energy balance closure problem: An overview. Ecological Applications, 18(6),
939 1351-1367.doi:10.1890/06-0922.1

940 French, A. N., Hunsaker, D. J., & Thorp, K. R. (2015). Remote sensing of evapotranspiration over
941 cotton using the TSEB and METRIC energy balance models. Remote Sensing of Environment, 158,
942 281–294. doi:10.1016/j.rse.2014.11.003

943 Funk, C., Peterson, P., Landsfeld, M., Pedreros, D., Verdin, J., Shukla, S., ... & Michaelsen, J. (2015).
944 The climate hazards infrared precipitation with stations—a new environmental record for monitoring
945 extremes. Scientific data, 2(1), 1-21. doi:10.1038/sdata.2015.66

946 Gan, R., Zhang, Y., Shi, H., Yang, Y., Eamus, D., Cheng, L., … Yu, Q. (2018). Use of satellite leaf
947 area index estimating evapotranspiration and gross assimilation for Australian ecosystems.
948 Ecohydrology, 11(5), e1974. doi:10.1002/eco.1974

949 Gokmen, M., Vekerdy, Z., Verhoef, A., Verhoef, W., Batelaan, O., & van der Tol, C. (2012).
950 Integration of soil moisture in SEBS for improving evapotranspiration estimation under water stress
951 conditions. Remote Sensing of Environment, 121, 261–274. doi:10.1016/j.rse.2012.02.003

952 Gorelick, N., Hancher, M., Dixon, M., Ilyushchenko, S., Thau, D., & Moore, R. (2017). Google Earth
953 Engine: Planetary-scale geospatial analysis for everyone. Remote Sensing of Environment, 202,
954 18–27. doi:10.1016/j.rse.2017.06.031

955 Gupta, H. V., Sorooshian, S., & Yapo, P. O. (1999). Status of automatic calibration for hydrologic
956 models: Comparison with multilevel expert calibration. Journal of hydrologic engineering, 4(2), 135-
957 143. doi:10.1061/(ASCE)1084-0699(1999)4:2(135)

958 Hallak, R. & Pereira Filho, A. J. (2011). Metodologia para análise de desempenho de simulações de
959 sistemas convectivos na região metropolitana de São Paulo com o modelo ARPS: sensibilidade a

variações com os esquemas de advecção e assimilação de dados. Revista Brasileira de Meteorologia, 26, 591-608.doi:10.1590/S0102-77862011000400009

Hollinger, D. Y., & Richardson, A. D. (2005). Uncertainty in eddy covariance measurements and its application to physiological models. Tree Physiology, 25(7), 873–885. doi:10.1093/treephys/25.7.873

Jaafar, H., Mourad, R., & Schull, M. (2022). A global 30-m ET model (HSEB) using harmonized Landsat and Sentinel-2, MODIS and VIIRS: Comparison to ECOSTRESS ET and LST. Remote Sensing of Environment, 274, 112995. doi:10.1016/j.rse.2022.112995

Jia, L., Su, Z., van den Hurk, B., Menenti, M., Moene, A., De Bruin, H. A. ., … Cuesta, A. (2003). Estimation of sensible heat flux using the Surface Energy Balance System (SEBS) and ATSR measurements. Physics and Chemistry of the Earth, Parts A/B/C, 28(1-3), 75–88. doi:10.1016/s1474-7065(03)00009-3

Kayser, R. H., Ruhoff, A., Laipelt, L., de Mello Kich, E., Roberti, D. R., de Arruda Souza, V., ... & Neale, C. M. U. (2022). Assessing geeSEBAL automated calibration and meteorological reanalysis uncertainties to estimate evapotranspiration in subtropical humid climates. Agricultural and Forest Meteorology, 314, 108775. doi:10.1016/j.agrformet.2021.108775

Koch, R., Almeida-Cortez, J. S., & Kleinschmit, B. (2017). Revealing areas of high nature conservation importance in a seasonally dry tropical forest in Brazil: Combination of modelled plant diversity hot spots and threat patterns. Journal for Nature Conservation, 35, 24–39. doi:10.1016/j.jnc.2016.11.004

Kustas, W., Choudhury, B. Moran, M., Reginato, R., Jackson, R., Gay, L., & Weaver, H. (1989a). Determination of sensible heat flux over sparse canopy using thermal infrared data. Agricultural and Forest Meteorology, 44(3-4), 197–216. doi:10.1016/0168-1923(89)90017-8

983 Kustas, W. P., Choudhury, B. J., Kunkel, K. E., & Gay, L. W. (1989b). Estimate of the aerodynamic
984 roughness parameters over an incomplete canopy cover of cotton. Agricultural and Forest
985 Meteorology, 46(1-2), 91-105. doi:10.1016/0168-1923(89)90114-7

986 Laipelt, L., Ruhoff, A. L., Fleischmann, A. S., Kayser, R. H. B., Kich, E. de M., da Rocha, H. R., &
987 Neale, C. M. U. (2020). Assessment of an Automated Calibration of the SEBAL Algorithm to Estimate
988 Dry-Season Surface-Energy Partitioning in a Forest–Savanna Transition in Brazil. Remote Sensing,
989 12(7), 1108. doi:10.3390/rs12071108

990 Laipelt, L., Henrique Bloedow Kayser, R., Santos Fleischmann, A., Ruhoff, A., Bastiaanssen, W.,
991 Erickson, T. A., & Melton, F. (2021). Long-term monitoring of evapotranspiration using the SEBAL
992 algorithm and Google Earth Engine cloud computing. ISPRS Journal of Photogrammetry and
993 Remote Sensing, 178, 81–96. doi:10.1016/j.isprsjprs.2021.05.018

994 Lhomme, J. P., Chehbouni, A., & Monteny, B. (2000). Sensible Heat Flux-Radiometric Surface
995 Temperature Relationship Over Sparse Vegetation: Parameterizing B-1. Boundary-Layer
996 Meteorology, 97(3), 431–457. doi:10.1023/a:1002786402695

997 Liao, J. J., & Lewis, J. W. (2000). A note on concordance correlation coefficient. PDA Journal of
998 Pharmaceutical Science and Technology, 54(1), 23-26.

999 Lima, A. L. A., & Rodal, M. J. N. (2010). Phenology and wood density of plants growing in the semi-
1000 arid region of northeastern Brazil. Journal of Arid Environments, 74(11), 1363–1373.
1001 doi:10.1016/j.jaridenv.2010.05.009

1002 Lima, A. L. A., Sá Barretto Sampaio, E. V., Castro, C. C., Rodal, M. J. N., Antonino, A. C. D., & de
1003 Melo, A. L. (2012). Do the phenology and functional stem attributes of woody species allow for the
1004 identification of functional groups in the semiarid region of Brazil? Trees, 26(5), 1605–1616.
1005 doi:10.1007/s00468-012-0735-2

1006 Lima, C. E. S. de, Costa, V. S. de O., Galvíncio, J. D., Silva, R. M. da, & Santos, C. A. G. (2021).
1007 Assessment of automated evapotranspiration estimates obtained using the GP-SEBAL algorithm for

1008 dry forest vegetation (Caatinga) and agricultural areas in the Brazilian semiarid region. Agricultural
1009 Water Management, 250, 106863. doi:10.1016/j.agwat.2021.106863

1010 Lin, L. K. (1989). A concordance correlation coefficient to evaluate reproducibility. Biometrics, 45(1),
1011 255–268. https://doi.org/10.2307/2532051

1012 Liu, S., Lu, L., Mao, D., & Jia, L. (2007). Evaluating parameterizations of aerodynamic resistance to
1013 heat transfer using field measurements. Hydrology and Earth System Sciences, 11(2), 769–783.
1014 doi:10.5194/hess-11-769-2007

1015 Liu, Y., Guo, W., Huang, H., Ge, J., & Qiu, B. (2021). Estimating global aerodynamic parameters in
1016 1982–2017 using remote-sensing data and a turbulent transfer model. Remote Sensing of
1017 Environment, 260, 112428. doi:10.1016/j.rse.2021.112428

1018 Long, D., Gao, Y., & Singh, V. P. (2010). Estimation of daily average net radiation from MODIS data
1019 and DEM over the Baiyangdian watershed in North China for clear sky days. Journal of Hydrology,
1020 388(3–4), 217–233. doi:10.1016/j.jhydrol.2010.04.042

1021 Long, D., Singh, V. P., & Li, Z.-L. (2011). How sensitive is SEBAL to changes in input variables,
1022 domain size and satellite sensor? Journal of Geophysical Research: Atmospheres, 116(D21).
1023 Portico. doi:10.1029/2011jd016542

1024 Maia, V. A., de Souza, C. R., de Aguiar-Campos, N., Fagundes, N. C. A., Santos, A. B. M., de Paula,
1025 G. G. P., … dos Santos, R. M. (2020). Interactions between climate and soil shape tree community
1026 assembly and above-ground woody biomass of tropical dry forests. Forest Ecology and
1027 Management, 474, 118348. doi:10.1016/j.foreco.2020.118348

1028 Mallick, K., Wandera, L., Bhattarai, N., Hostache, R., Kleniewska, M., & Chormanski, J. (2018). A
1029 critical evaluation on the role of aerodynamic and canopy–surface conductance parameterization in
1030 SEB and SVAT models for simulating evapotranspiration: A case study in the Upper Biebrza National
1031 Park Wetland in Poland. Water, 10(12), 1753. doi.org/10.3390/w10121753

Marques, T. V., Mendes, K., Mutti, P., Medeiros, S., Silva, L., Perez-Marin, A. M., … Bezerra, B. (2020). Environmental and biophysical controls of evapotranspiration from Seasonally Dry Tropical Forests (Caatinga) in the Brazilian Semiarid. Agricultural and Forest Meteorology, 287, 107957. doi:10.1016/j.agrformet.2020.107957

McShane, R. R., Driscoll, K. P., & Sando, R. (2017). A review of surface energy balance models for estimating actual evapotranspiration with remote sensing at high spatiotemporal resolution over large extents. Scientific Investigations Report. doi:10.3133/sir20175087

Medeiros, R., Andrade, J., Ramos, D., Moura, M., Pérez-Marin, A., dos Santos, C., … Cunha, J. (2022). Remote Sensing Phenology of the Brazilian Caatinga and Its Environmental Drivers. Remote Sensing, 14(11), 2637. doi:10.3390/rs14112637

Melo, D. C. D., Anache, J. A. A., Borges, V. P., Miralles, D. G., Martens, B., Fisher, J. B., … Wendland, E. (2021). Are remote sensing evapotranspiration models reliable across South American ecoregions? Water Resources Research, 57(11). doi:10.1029/2020wr028752

Mhawej, M., Caiserman, A., Nasrallah, A., Dawi, A., Bachour, R., & Faour, G. (2020). Automated evapotranspiration retrieval model with missing soil-related datasets: The proposal of SEBALI. Agricultural Water Management, 229, 105938. doi:10.1016/j.agwat.2019.105938

Miles, L., Newton, A. C., DeFries, R. S., Ravilious, C., May, I., Blyth, S., … Gordon, J. E. (2006). A global overview of the conservation status of tropical dry forests. Journal of Biogeography, 33(3), 491–505. doi:10.1111/j.1365-2699.2005.01424.x

Miranda, R. Q., Nóbrega, R. L. B., Moura, M. S. B., Raghavan, S., & Galvíncio, J. D. (2020). Realistic and simplified models of plant and leaf area indices for a seasonally dry tropical forest. International Journal of Applied Earth Observation and Geoinformation, 85, 101992. doi:10.1016/j.jag.2019.101992

1055 Miranda, R. D. Q., Galvincio, J. D., Morais, Y. C. B., Moura, M. S. B. D., Jones, C. A., & Srinivasan,
1056 R. (2018). Dry forest deforestation dynamics in Brazil's Pontal Basin. Revista Caatinga, 31, 385-395.
1057 doi:10.1590/1983-21252018v31n215rc

1058 Mohan, M. M. P., Kanchirapuzha, R., & Varma, M. R. R. (2020a). Review of approaches for the
1059 estimation of sensible heat flux in remote sensing-based evapotranspiration models. Journal of
1060 Applied Remote Sensing, 14(04). doi:10.1117/1.jrs.14.041501

1061 Mohan, M. P.; Kanchirapuzha, R., & Varma, M. R. R. (2020b). Integration of soil moisture as an
1062 auxiliary parameter for the anchor pixel selection process in SEBAL using Landsat 8 and Sentinel-
1063 1A images. International Journal of Remote Sensing, 41(3), 1214-1231.

1064 Moro, M. F., Silva, I. A., Araújo, F. S. de, Nic Lughadha, E., Meagher, T. R., & Martins, F. R. (2015).
1065 The role of edaphic environment and climate in structuring phylogenetic pattern in Seasonally Dry
1066 Tropical Plant Communities. PLOS ONE, 10(3), e0119166. doi:10.1371/journal.pone.0119166

1067 Moro, M. F., Nic Lughadha, E., de Araújo, F. S., & Martins, F. R. (2016). A Phytogeographical
1068 Metaanalysis of the Semiarid Caatinga domain in Brazil. The Botanical Review, 82(2), 91–148.
1069 doi:10.1007/s12229-016-9164-z

1070 Mu, Q., Zhao, M., & Running, S. W. (2011). Improvements to a MODIS global terrestrial
1071 evapotranspiration algorithm. Remote Sensing of Environment, 115(8), 1781–1800.
1072 doi:10.1016/j.rse.2011.02.019

1073 Muñoz Sabater, J., (2019): ERA5-Land hourly data from 1981 to present. Copernicus Climate
1074 Change Service (C3S) Climate Data Store (CDS). (Accessed on 23-Feb-2022),
1075 doi:10.24381/cds.e2161bac

1076 Mutti, P. R., da Silva, L. L., Medeiros, S. de S., Dubreuil, V., Mendes, K. R., Marques, T. V., …
1077 Bezerra, B. G. (2019). Basin scale rainfall-evapotranspiration dynamics in a tropical semiarid
1078 environment during dry and wet years. International Journal of Applied Earth Observation and
1079 Geoinformation, 75, 29–43. doi:10.1016/j.jag.2018.10.007

1080 Murray, T., and Verhoef, A. (2007) Moving towards a more mechanistic approach in the
1081 determination of soil heat flux from remote measurements. II. Diurnal shape of soil heat flux.
1082 Agricultural and Forest Meteorology, 147: 88-97.

1083 Nash, J. E., & Sutcliffe, J. V. (1970). River flow forecasting through conceptual models part I - A
1084 discussion of principles. Journal of Hydrology, 10(3), 282–290. doi:10.1016/0022-1694(70)90255-6

1085 Oliveira, M. L., Santos, C. A. C., Oliveira, G., Perez-Marin, A. M., & Santos, C. A. G. (2021). Effects
1086 of human-induced land degradation on water and carbon fluxes in two different Brazilian dryland soil
1087 covers. Science of the Total Environment, 792, 148458. doi:10.1016/j.scitotenv.2021.148458

1088 Owen, P. R., & Thomson, W. R. (1963). Heat transfer across rough surfaces. Journal of Fluid
1089 Mechanics, 15(3), 321–334. doi:10.1017/s0022112063000288

1090 Paloschi, R. A., Ramos, D. M., Ventura, D. J., Souza, R., Souza, E., Morellato, L. P. C., … Borma,
1091 L. D. S. (2020). Environmental drivers of water use for Caatinga woody plant species: Combining
1092 remote sensing phenology and sap flow measurements. Remote Sensing, 13(1), 75.
1093 doi:10.3390/rs13010075

1094 Paul, G., Gowda, P. H., Vara Prasad, P. V., Howell, T. A., Staggenborg, S. A., & Neale, C. M. U.
1095 (2013). Lysimetric evaluation of SEBAL using high resolution airborne imagery from BEAREX08.
1096 Advances in Water Resources, 59, 157–168. doi:10.1016/j.advwatres.2013.06.003

1097 Paul, G., Gowda, P. H., Vara Prasad, P. V., Howell, T. A., Aiken, R. M., & Neale, C. M. U. (2014).
1098 Investigating the influence of roughness length for heat transport (zoh) on the performance of SEBAL
1099 in semi-arid irrigated and dryland agricultural systems. Journal of Hydrology, 509, 231–244.
1100 doi:10.1016/j.jhydrol.2013.11.040

1101 Paulson, C. A. (1970). The mathematical representation of wind speed and temperature profiles in
1102 the unstable atmospheric surface layer. Journal of Applied Meteorology and Climatology, 9(6), 857-
1103 861. doi:10.1175/1520-0450(1970)009%3C0857:tmrows%3E2.0.co;2

Pennington, R. T., Lewis, G. P., & Ratter, J. A. (Eds.). (2006). An overview of the plant diversity, biogeography and conservation of Neotropical Savannas and Seasonally Dry Forests. Neotropical Savannas and Seasonally Dry Forests, 1–29. doi:10.1201/9781420004496-1

Pennington, R. T., Lavin, M., & Oliveira-Filho, A. (2009). Woody plant diversity, evolution, and ecology in the Tropics: Perspectives from Seasonally Dry Tropical Forests. Annual Review of Ecology, Evolution, and Systematics, 40(1), 437–457. doi:10.1146/annurev.ecolsys.110308.120327

Pennington, R. T., Lehmann, C. E. R., & Rowland, L. M. (2018). Tropical savannas and dry forests. Current Biology, 28(9), R541–R545. doi:10.1016/j.cub.2018.03.014

Potapov, P., Li, X., Hernandez-Serna, A., Tyukavina, A., Hansen, M. C., Kommareddy, A., … Hofton, M. (2021). Mapping global forest canopy height through integration of GEDI and Landsat data. Remote Sensing of Environment, 253, 112165. doi:10.1016/j.rse.2020.112165

Priestley, C. H. B., & Taylor, R. J. (1972). On the assessment of surface heat flux and evaporation using large-scale parameters. Monthly Weather Review, 100(2), 81–92. doi:10.1175/1520-0493(1972)100<0081:otaosh>2.3.co;2

Queiroz, L. P., Cardoso, D., Fernandes, M. F., & Moro, M. F. (2017). Diversity and evolution of flowering plants of the Caatinga domain. Caatinga, 23–63. doi:10.1007/978-3-319-68339-3_2

Queiroz, M. G. D., Silva, T. G. F. D., Souza, C. A. A. D., Jardim, A. M. D. R. F., Araújo Júnior, G. D. N., Souza, L. S. B. D., & Moura, M. S. B. D. (2020). Composition of Caatinga species under anthropic disturbance and its correlation with rainfall partitioning. Floresta e Ambiente, 28. doi:10.1590/2179-8087-FLORAM-2019-0044

Ramoelo, A., Majozi, N., Mathieu, R., Jovanovic, N., Nickless, A., & Dzikiti, S. (2014). Validation of global evapotranspiration product (MOD16) using flux tower data in the African Savanna, South Africa. Remote Sensing, 6(8), 7406–7423. doi:10.3390/rs6087406

Rasp, S., Pritchard, M. S., & Gentine, P. (2018). Deep learning to represent subgrid processes in climate models. Proceedings of the National Academy of Sciences, 115(39), 9684–9689. doi:10.1073/pnas.1810286115

Raupach, M. R. (1992). Drag and drag partition on rough surfaces. Boundary-Layer Meteorology, 60(4), 375–395. doi.org/10.1007/bf00155203

Raupach, M. R. (1994). Simplified expressions for vegetation roughness length and zero-plane displacement as functions of canopy height and area index. Boundary-Layer Meteorology, 71(1–2), 211–216. doi:10.1007/bf00709229

Roberts, W., Williams, G. P., Jackson, E., Nelson, E. J., & Ames, D. P. (2018). Hydrostats: A Python package for characterizing errors between observed and predicted time series. Hydrology, 5(4), 66. doi:10.3390/hydrology5040066

Rodell, M., Houser, P. R., Jambor, U., Gottschalck, J., Mitchell, K., Meng, C.-J., … Toll, D. (2004). The Global Land Data Assimilation System. Bulletin of the American Meteorological Society, 85(3), 381–394. doi:10.1175/bams-85-3-381

Running, S., Mu, Q., Zhao, M. (2017). MOD16A2 MODIS/Terra Net Evapotranspiration 8-Day L4 Global 500m SIN Grid V006 [Data set]. NASA EOSDIS Land Processes DAAC. Accessed 23-Feb-2022 from doi:10.5067/MODIS/MOD16A2.006

Sahnoun, F., Abderrahmane, H., Kaddour, M., Abdelkader, K., Mohamed, B., & Castro, T. A. H. D. (2021). Application of SEBAL and T s/VI trapezoid models for estimating actual evapotranspiration in the Algerian Semi-Arid Environment to improve agricultural water management. Revista Brasileira de Meteorologia, 36, 219-236. doi:10.1590/0102-77863610020

Salazar-Martínez, D., Holwerda, F., Holmes, T. R. H., Yépez, E. A., Hain, C. R., Alvarado-Barrientos, S., … Vivoni, E. R. (2022). Evaluation of remote sensing-based evapotranspiration products at low-latitude eddy covariance sites. Journal of Hydrology, 610, 127786. doi:10.1016/j.jhydrol.2022.127786

Santos, R. M., Oliveira-Filho, A. T., Eisenlohr, P. V., Queiroz, L. P., Cardoso, D. B. O. S., & Rodal, M. J. N. (2012). Identity and relationships of the Arboreal Caatinga among other floristic units of seasonally dry tropical forests (SDTFs) of north-eastern and Central Brazil. Ecology and Evolution, 2(2), 409–428. doi:10.1002/ece3.91

Santos, M. G., Oliveira, M. T., Figueiredo, K. V., Falcão, H. M., Arruda, E. C. P., Almeida-Cortez, J., … Antonino, A. C. D. (2014). Caatinga, the Brazilian dry tropical forest: can it tolerate climate changes? Theoretical and Experimental Plant Physiology, 26(1), 83–99. doi:10.1007/s40626-014-0008-0

Santos, C. A. C., Mariano, D. A., das Chagas A. do Nascimento, F., da C. Dantas, F. R., de Oliveira, G., Silva, M. T., … Neale, C. M. U. (2020). Spatio-temporal patterns of energy exchange and evapotranspiration during an intense drought for drylands in Brazil. International Journal of Applied Earth Observation and Geoinformation, 85, 101982. doi:10.1016/j.jag.2019.101982

Schaaf, C., & Wang, Z. (2015). MCD43A4 MODIS/Terra+Aqua BRDF/Albedo Nadir BRDF Adjusted Ref Daily L3 Global - 500m V006 [Data set]. NASA EOSDIS Land Processes DAAC. Accessed 23-Feb-2022. doi:10.5067/MODIS/MCD43A4.006

Senay, G. B., Bohms, S., Singh, R. K., Gowda, P. H., Velpuri, N. M., Alemu, H., & Verdin, J. P. (2013). Operational evapotranspiration mapping using remote sensing and weather datasets: A new parameterization for the SSEB approach. JAWRA Journal of the American Water Resources Association, 49(3), 577–591. Portico. https://doi.org/10.1111/jawr.12057

Senay, G. B., Friedrichs, M., Morton, C., Parrish, G. E., Schauer, M., Khand, K., ... & Huntington, J. (2022). Mapping actual evapotranspiration using Landsat for the conterminous United States: Google Earth Engine implementation and assessment of the SSEBop model. Remote Sensing of Environment, 275, 113011. doi:10.1016/j.rse.2022.113011

Senkondo, W., Munishi, S. E., Tumbo, M., Nobert, J., & Lyon, S. W. (2019). Comparing remotely-sensed surface energy balance evapotranspiration estimates in heterogeneous and data-limited

1177 regions: a case study of Tanzania's Kilombero Valley. Remote Sensing, 11(11), 1289.
1178 doi:10.3390/rs11111289

1179 Shuttleworth, W. J. (2012). Terrestrial hydrometeorology. John Wiley & Sons.

1180 Silva, A. M., da Silva, R. M., & Santos, C. A. G. (2019). Automated surface energy balance algorithm
1181 for land (ASEBAL) based on automating endmember pixel selection for evapotranspiration
1182 calculation in MODIS orbital images. International Journal of Applied Earth Observation and
1183 Geoinformation, 79, 1–11. doi:10.1016/j.jag.2019.02.012

1184 Silva, J. M. C.; LEAL, I.R.; Tabarelli, M. (Ed.). (2017a). Caatinga: the largest tropical dry forest region
1185 in South America. Springer.

1186 Silva, P. F. da, Lima, J. R. de S., Antonino, A. C. D., Souza, R., Souza, E. S. de, Silva, J. R. I., &
1187 Alves, E. M. (2017b). Seasonal patterns of carbon dioxide, water and energy fluxes over the
1188 Caatinga and grassland in the semi-arid region of Brazil. Journal of Arid Environments, 147, 71–82.
1189 doi:10.1016/j.jaridenv.2017.09.003

1190 Singh, R. K., & Irmak, A. (2011). Treatment of anchor pixels in the METRIC model for improved
1191 estimation of sensible and latent heat fluxes. Hydrological Sciences Journal, 56(5), 895–906.
1192 doi:10.1080/02626667.2011.587424

1193 Singh, R. K., Liu, S., Tieszen, L. L., Suyker, A. E., & Verma, S. B. (2012). Estimating seasonal
1194 evapotranspiration from temporal satellite images. Irrigation Science, 30(4), 303-313.
1195 doi:10.1007/s00271-011-0287-z

1196 Souza, L. S. B. de, Moura, M. S. B. de, Sediyama, G. C., & Silva, T. G. F. da. (2015). Balanço de
1197 energia e controle biofísico da evapotranspiração na Caatinga em condições de seca intensa.
1198 Pesquisa Agropecuária Brasileira, 50(8), 627–636. doi:10.1590/s0100-204x2015000800001

1199 Stewart, J. B., Kustas, W. P., Humes, K. S., Nichols, W. D., Moran, M. S., & de Bruin, H. A. (1994).
1200 Sensible heat flux-radiometric surface temperature relationship for eight semiarid areas. Journal of

1201 Applied Meteorology and Climatology, 33(9), 1110-1117. doi:10.1175/1520-
1202 0450(1994)033%3C1110:shfrst%3E2.0.co;2

1203 Su, Z., Schmugge, T., Kustas, W. P., & Massman, W. J. (2001). An evaluation of two models for
1204 estimation of the roughness height for heat transfer between the land surface and the atmosphere.
1205 Journal of Applied Meteorology, 40(11), 1933-1951. doi:10.1175/1520-
1206 0450(2001)040%3C1933:aeotmf%3E2.0.co;2

1207 Su, Z. (2002). The Surface Energy Balance System (SEBS) for estimation of turbulent heat fluxes.
1208 Hydrology and Earth System Sciences, 6(1), 85–100. doi:10.5194/hess-6-85-2002

1209 Teixeira, A. D. C., Bastiaanssen, W. G., Ahmad, M., & Bos, M. G. (2009). Reviewing SEBAL input
1210 parameters for assessing evapotranspiration and water productivity for the Low-Middle Sao
1211 Francisco River basin, Brazil: Part A: Calibration and validation. Agricultural and Forest Meteorology,
1212 149(3-4), 462-476. doi:10.1016/j.agrformet.2008.09.016

1213 Thom, A. S. (1972). Momentum, mass and heat exchange of vegetation. Quarterly Journal of the
1214 Royal Meteorological Society, 98(415), 124–134. doi:10.1002/qj.49709841510

1215 Tomasella, J., Silva Pinto Vieira, R. M., Barbosa, A. A., Rodriguez, D. A., Oliveira Santana, M. de, &
1216 Sestini, M. F. (2018). Desertification trends in the Northeast of Brazil over the period 2000–2016.
1217 International Journal of Applied Earth Observation and Geoinformation, 73, 197–206.
1218 doi:10.1016/j.jag.2018.06.012

1219 Trebs, I., Mallick, K., Bhattarai, N., Sulis, M., Cleverly, J., Woodgate, W., Silberstein, R., Hinko-
1220 Najera, N., Beringer, J., Su, Z., & Boulet, G. (2021). The role of aerodynamic resistance in thermal
1221 remote sensing-based evapotranspiration models. EGU General Assembly.
1222 doi.org/10.5194/egusphere-egu21-2186

1223 Trezza, R. (2006). Evapotranspiration from a remote sensing model for water management in an
1224 irrigation system in Venezuela. Interciencia, 31(6), 417-423

1225 Trezza, R., Allen, R., & Tasumi, M. (2013). Estimation of Actual Evapotranspiration along the Middle
1226 Rio Grande of New Mexico Using MODIS and Landsat Imagery with the METRIC Model. Remote
1227 Sensing, 5(10), 5397–5423. doi:10.3390/rs5105397

1228 Troufleau, D., Lhomme, J. P., Monteny, B., & Vidal, A. (1997). Sensible heat flux and radiometric
1229 surface temperature over sparse Sahelian vegetation. I. An experimental analysis of the kB−1
1230 parameter. Journal of Hydrology, 188, 815-838. doi:10.1016/s0022-1694(96)03172-1

1231 Verhoef, A., De Bruin, H. A. R., & Van Den Hurk, B. J. J. M. (1997a). Some practical notes on the
1232 parameter kB−1 for sparse vegetation. Journal of Applied Meteorology, 36(5), 560-572.
1233 doi:10.1175/1520-0450(1997)036%3C0560:spnotp%3E2.0.co;2

1234 Verhoef, A., McNaughton, K. G., & Jacobs, A. F. G. (1997b). A parameterization of momentum
1235 roughness length and displacement height for a wide range of canopy densities. Hydrology and Earth
1236 System Sciences, 1(1), 81–91. doi:10.5194/hess-1-81-1997

1237 Wang, C., Yang, J., Myint, S. W., Wang, Z.-H., & Tong, B. (2016). Empirical modeling and spatio-
1238 temporal patterns of urban evapotranspiration for the Phoenix metropolitan area, Arizona. GIScience
1239 & Remote Sensing, 53(6), 778–792. doi:10.1080/15481603.2016.1243399

1240 Wilson, K., Goldstein, A., Falge, E., Aubinet, M., Baldocchi, D., Berbigier, P., … Verma, S. (2002).
1241 Energy balance closure at FLUXNET sites. Agricultural and Forest Meteorology, 113(1-4), 223–243.
1242 doi:10.1016/s0168-1923(02)00109-0

1243 WRB, I.W.G., 2006. World reference base for soil resources 2006, 2nd ed. In: FAO (ed.), World Soil
1244 Resources Reports No. 103, Rome. ISBN 92-5-105511-4.

1245 Wu, Q. (2020). geemap: A Python package for interactive mapping with Google Earth Engine.
1246 Journal of Open Source Software, 5(51), 2305. doi:10.21105/joss.02305

1247 Yin, L., Wang, X., Feng, X., Fu, B., & Chen, Y. (2020). A comparison of SSEBop-Model-Based
1248 evapotranspiration with eight evapotranspiration products in the Yellow River Basin, China. Remote
1249 Sensing, 12(16), 2528. doi:10.3390/rs12162528

Zhang, Y., Kong, D., Gan, R., Chiew, F. H. S., McVicar, T. R., Zhang, Q., & Yang, Y. (2019). Coupled estimation of 500 m and 8-day resolution global evapotranspiration and gross primary production in 2002–2017. Remote Sensing of Environment, 222, 165–182. doi:10.1016/j.rse.2018.12.031

Zhao, M., Heinsch, F. A., Nemani, R. R., & Running, S. W. (2005). Improvements of the MODIS terrestrial gross and net primary production global data set. Remote sensing of Environment, 95(2), 164-176. doi:10.1016/j.rse.2004.12.011